



Originally published as:

Guanter, L., Brell, M., Chan, J.-C.-W., Giardino, C., Gomez-Dans, J., Mielke, C., Morsdorf, F., Segl, K., Yokoya, N. (2019): Synergies of Spaceborne Imaging Spectroscopy with Other Remote Sensing Approaches. - *Surveys in Geophysics*, 40, 3, pp. 657—687.

DOI: <http://doi.org/10.1007/s10712-018-9485-z>

# 1 Synergies of Spaceborne Imaging Spectroscopy with other Remote 2 Sensing Approaches

3 Luis Guanter<sup>1</sup>, Maximilian Brell<sup>1</sup>, Jonathan C.-W. Chan<sup>2</sup>,  
4 Claudia Giardino<sup>3</sup>, Jose Gomez-Dans<sup>4</sup>, Christian Mielke<sup>1</sup>,  
5 Felix Morsdorf<sup>5</sup>, Karl Segl<sup>1</sup>, Naoto Yokoya<sup>6</sup>

6  
7 <sup>1</sup>Helmholtz Centre Potsdam German Centre for Geosciences (GFZ), Potsdam, Germany

8 <sup>2</sup>Department of Electronics and Informatics, Vrije Universiteit Brussel, Brussels, Belgium

9 <sup>3</sup>CNR-IREA, Institute for Electromagnetic Sensing of the Environment, Milan, Italy

10 <sup>4</sup>Department of Geography and National Centre for Earth Observation, University College London, UK

11 <sup>5</sup>Remote Sensing Laboratories, Department of Geography, University of Zurich, Switzerland

12 <sup>6</sup>RIKEN Center for Advanced Intelligence Project, Tokyo, Japan

13 **Abstract** Imaging spectroscopy (IS), also commonly known as hyperspectral remote sensing, is a powerful  
14 remote sensing technique for the monitoring of the Earth's surface and atmosphere. Pixels in optical hyper-  
15 spectral images consist of continuous reflectance spectra formed by hundreds of narrow spectral channels,  
16 allowing an accurate representation of the surface composition through spectroscopic techniques. However,  
17 technical constraints in the definition of imaging spectrometers make spectral coverage and resolution to  
18 be usually traded by spatial resolution and swath width, as opposed to optical multispectral (MS) systems  
19 typically designed to maximize spatial and/or temporal resolution. This complementarity suggests that a  
20 synergistic exploitation of spaceborne IS and MS data would be an optimal way to fulfill those remote  
21 sensing applications requiring not only high spatial and temporal resolution data, but also rich spectral in-  
22 formation. On the other hand, IS has been shown to yield a strong synergistic potential with non-optical  
23 remote sensing methods, such as thermal infrared (TIR) and light detection and ranging (LiDAR). In this  
24 contribution we review theoretical and methodological aspects of potential synergies between optical IS  
25 and other remote sensing techniques. The focus is put on the evaluation of synergies between spaceborne  
26 optical IS and MS systems because of the expected availability of the two types of data in the next years.  
27 Short reviews of potential synergies of IS with TIR and LiDAR measurements are also provided.

28 **Keywords** Imaging spectroscopy · multispectral remote sensing · synergy · data fusion · spatial  
29 enhancement · thermal infrared · LiDAR

## 30 1 Introduction

31 Imaging spectroscopy (IS) in the optical domain, also known as hyperspectral remote sensing, is an Earth  
32 observation technique based on spectrally-contiguous measurements of the solar light reflected by the

---

L. Guanter  
Helmholtz Centre Potsdam German Centre for Geosciences (GFZ)  
Telegrafenberg A17 14473 Potsdam, Germany  
Tel.: +49-3312881190  
Fax: +49-3312881192  
E-mail: guanter@gfz-potsdam.de

Earth's surface and atmosphere (Goetz et al., 1985). Each pixel in the resulting hyperspectral images contains a continuous spectrum sampling absorption features which can be linked to the pixel composition. Due to this generic measurement principle, IS provides an accurate representation of geobiophysical parameters, which can be used to infer quantitative information on a wide range of Earth's surface parameters and processes.

The rise and consolidation of IS as a powerful remote sensing technique for land monitoring over the last three decades has mostly relied on airborne spectrometers. In particular, the NASA Jet Propulsion Laboratory's Airborne Visible/Infrared Imaging Spectrometer (AVIRIS) (Green et al., 1998), covering the 400–2500 nm spectral range (visible to shortwave infrared, VSWIR) with 10-nm wide spectral channels, has been used in a large number of campaigns across different continents and ecosystems (e.g. Thompson et al., 2017). From a satellite perspective, the Hyperion spectrometer onboard NASA's Earth Observing One (EO-1) spacecraft was a technology demonstration project which operated between 2001 and 2017 (Ungar et al., 2003). Hyperion acquired hyperspectral images with a 30 m ground sampling distance (GSD), a 7 km horizontal swath and a spectral coverage and sampling similar to that of AVIRIS, although with a much lower radiometric performance and overall data quality. Other satellite IS projects, in this case restricted to the visible near-infrared (VNIR, 400–1000 nm) spectral region, are the Compact High Resolution Imaging Spectrometer (CHRIS) on ESA's Proba-1 microsatellite (Barnsley et al., 2004), which has been operating since 2001, and the Hyperspectral Imager for the Coastal Ocean (HICO) (Lucke et al., 2011), developed by NASA and the US Office of Naval Research and operating onboard the International Space Station (ISS) between 2009 and 2015.

After those technology demonstration projects, several scientific missions expected to deliver accurate spectroscopic measurements are scheduled for the next years. In particular, the Environmental Mapping and Analysis Program (EnMAP) is a German mission which will measure in the VSWIR spectral range with an average spectral sampling of 10 nm, a 30 m GSD, a 30 km swath width and a revisit time under quasi-nadir observation of less than 4 weeks (Guanter et al., 2015). These characteristics are shared by the Italian Space Agency's PRISMA (Hyperspectral Precursor of the Application Mission) (Candela et al., 2016), which in addition presents a panchromatic channel with a 5 m GSD. Other projects, such as NASA's Hyperspectral Infrared Imager (HyspIRI) (Lee et al., 2015), and the Italian-Israeli SHALOM (Spaceborne Hyperspectral Applicative Land and Ocean Mission), currently awaiting the final decision for implementation, could follow EnMAP and PRISMA by mid 2020s.

In general, upcoming space-based VSWIR IS missions such as EnMAP and PRISMA are expected to provide hyperspectral data in a higher data-rate and radiometric and spectral quality than their predecessor Hyperion. However, due to trade-offs in spectrometer design between spatial resolution, spectral resolution, swath width, and signal-to-noise ratio (SNR), spaceborne IS missions are usually designed to acquire data with a moderate GSD (typically 30 m) as well as with a small across-track swath, which results in a nadir revisit time of up to 4 weeks. It must also be mentioned that EnMAP and PRISMA are "site-oriented" missions, which means that they are tasked on a daily basis to acquire images over selected sites, as opposed to "wall-to-wall" mapping missions with systematic full global coverage. Temporal resolution will be improved by EnMAP and PRISMA through across-track pointing, but this can only happen over a limited number of sites per day due to the high impact of platform pointing maneuvers on mission operations. Those sampling limitations will hamper the use of EnMAP, PRISMA and similar missions for those applications requiring high temporal resolution (e.g. those dealing with water and vegetation) or spatial resolution (e.g. land cover mapping or mineral exploration).

The EnMAP and PRISMA spaceborne IS missions are expected to co-exist with a number of other satellite missions based on different measurement principles, and especially with optical multispectral (MS) missions. An overview of some operating and upcoming satellite missions mentioned in this paper is provided in Table 1. For example, the ESA/Copernicus Sentinel-2 mission (Drusch et al., 2012), which has an optical multispectral imager (MSI) as main payload, is planned for long-term operations and will coexist with EnMAP, PRISMA and other future IS missions. Sentinel-2 MSI has a wide spatial coverage (290 km

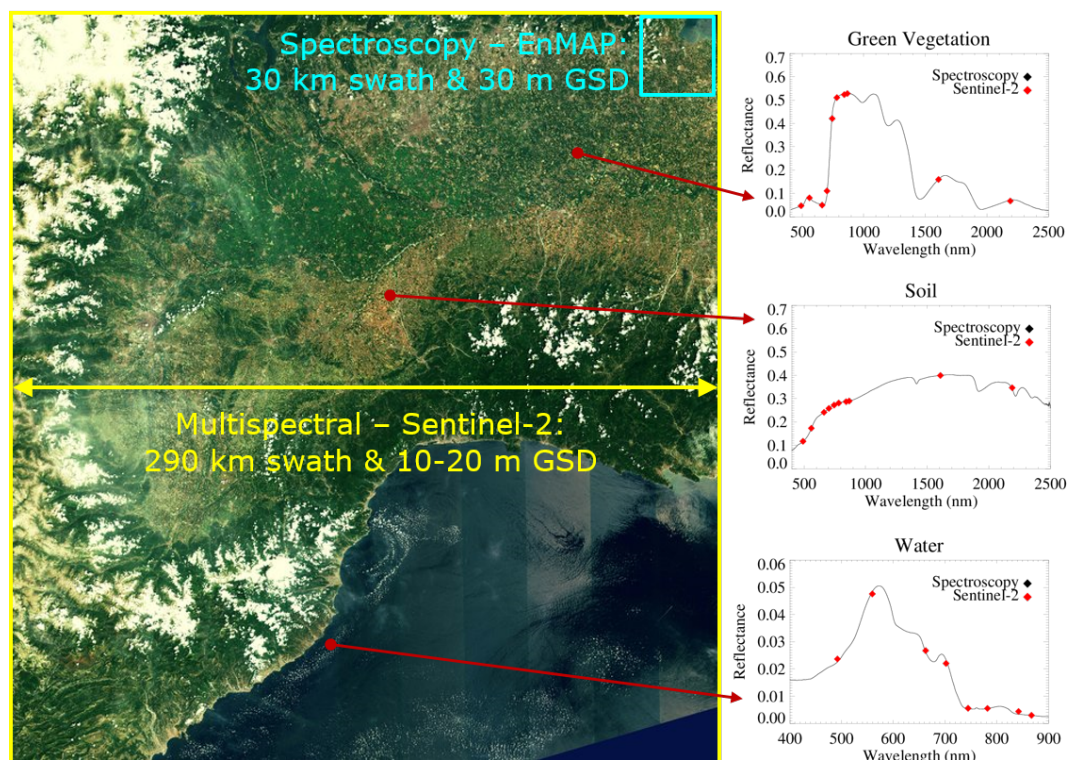


**Fig. 1** First image from Sentinel-2A covering parts of Italy and France in June 2015. The spatial coverage of Sentinel-2 is compared to that of the EnMAP imaging spectroscopy mission. Panels on the right hand side compare surface reflectance spectra as acquired by an imaging spectrometer and the 10–20 m channels in the multispectral imager (MSI) on Sentinel-2. GSD stands for ground sampling distance.

82 swath), VSWIR spectral coverage (13 spectral channels between 440 and 2200 nm), high spatial resolution  
 83 (10 spectral channels at 10 or 20 m ground sampling distance), high temporal resolution (5-day revisit time)  
 84 and open data policy. Also Landsat-8/9 missions (Roy et al., 2014) offer spatially continuous VSWIR MS  
 85 data and will co-exist with EnMAP and PRISMA. Optical MS missions such as Sentinel-2 and Landsat  
 86 hold a strong potential for synergistic use with EnMAP-like IS missions, since the poorer spectral infor-  
 87 mation of the multispectral data is compensated by their improved spatial coverage, temporal resolution,  
 88 and (in the case of Sentinel-2) spatial resolution. This is illustrated in Fig. 1. The combination of optical  
 89 IS and MS missions can thus be used for a temporal and/or spatial enhancement of the rich spectral infor-  
 90 mation provided by the IS data set. This is also the rationale for the inclusion of a panchromatic channel  
 91 in the PRISMA mission concept (Candela et al., 2016) and for the joint deployment of Hyperion and the  
 92 Advanced Land Imager (ALI) onboard the EO-1 platform.

93 A different type of synergy with IS data would be the one consisting in the combination of IS mea-  
 94 surements with those derived from non-optical instruments carrying fundamentally different information.  
 95 This would be, for instance, the combination of IS and light detection and ranging (LiDAR) data, which  
 96 can be very useful for e.g. the classification of urban objects or the characterization of vegetation covers.  
 97 The latter is main purpose of the Carnegie Airborne Observatory intended for ecological research, which  
 98 combines airborne spectroscopy and a dual-laser waveform LiDAR scanner (Asner et al., 2012). Regarding  
 99 other spectral ranges, the HypSIPI mission concept relies on the combination of spaceborne hyperspectral

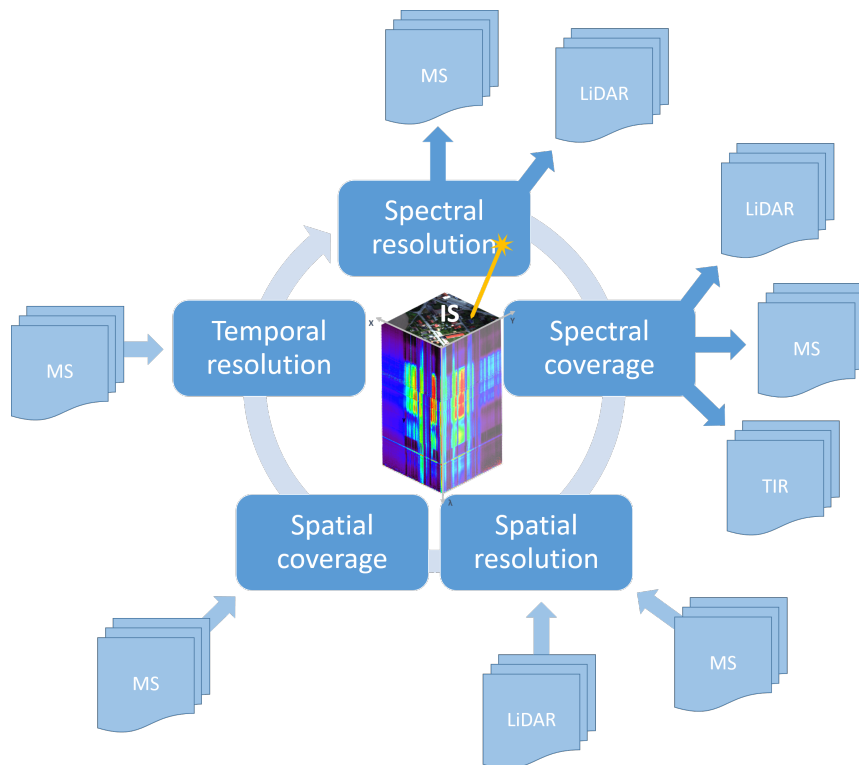


**Fig. 2** Schematic view of how synergies between imaging spectroscopy and other remote sensing techniques can be used to improve spectral, spatial and temporal sampling in the resulting data set. IS stands for imaging spectroscopy, MS for optical multispectral data and TIR for thermal infrared.

100 VSWIR and thermal infrared (TIR) measurements in order to address a number of scientific questions re-  
 101 lated to the Earth's ecosystems (Lee et al., 2015). Synergies between IS and TIR measurements are also  
 102 considered for the ESA FLUorescence EXplorer (FLEX) mission (Drusch et al., 2017). FLEX will provide  
 103 spectroscopic measurements in the 500–800 nm spectral window at high spectral resolution (<3 nm) and  
 104 low spatial resolution (GSD=300 m) for the retrieval of chlorophyll fluorescence and other plant biochem-  
 105 ical parameters. FLEX will fly in tandem with the Sentinel-3 mission adding TIR measurements necessary  
 106 for the interpretation of the fluorescence measurements from FLEX. On the other hand, an exceptional  
 107 wealth of information for ecosystem research will become available from the combined operation of a se-  
 108 ries of remote sensing instruments to be deployed at the ISS in 2018. This will include the Global Ecosystem  
 109 Dynamics Investigation (GEDI) LiDAR, the Ecosystem Spaceborne Thermal Radiometer Experiment on  
 110 Space Station (ECOSTRESS), and the Orbiting Carbon Observatory 3 (OCO-3), all three from NASA,  
 111 and the VSWIR Hyperspectral Imager Suite (HISUI) from the Japanese Ministry of Economy, Trade,  
 112 and Industry (METI). The combination of those four instruments will provide key information on canopy  
 113 structure (GEDI), evapotranspiration and stress (ECOSTRESS), chlorophyll fluorescence (OCO-3) and  
 114 ecosystem composition and plant traits (HISUI), which will be used to investigate vegetation functioning  
 115 at the ecosystem scale during the time period in which the 4 instruments will be operated (Stavros et al.,  
 116 2017).

117 This contribution reviews potential synergies between IS data and other remote sensing techniques. The  
 118 focus is on the discussion of theoretical aspects and methodological issues, rather than on a comprehensive

**Table 1** Observation parameters of some of the satellite missions mentioned in this paper. IS stands for imaging spectrometer, MS for multispectral instrument, VSWIR for visible to shortwave infrared, VNIR for visible near-infrared, SWIR for shortwave infrared, TIR for thermal infrared, GSD for ground sampling distance, PAN for panchromatic channel, and ALI for advance land imager.

	<b>Spectral sampling</b>	<b>Spectral coverage</b>	<b>GSD (optical)</b>	<b>Revisit time</b>	<b>Status</b>	<b>Note</b>
EnMAP	IS	VSWIR	30 m	27 d nadir, ~4 d with 30° pointing	Launch ~2020	Acquisitions on request
PRISMA	IS	VSWIR	30 m	29 d nadir, ~7 d with 15° pointing	Launch ~2018	Acquisitions on request; 5 m PAN
HypIRI	IS	VSWIR & TIR	30 m	5–16 d	Under evaluation	Global mapper with 185 km swath
Hyperion	IS	VSWIR	30 m	~6 d with 22° pointing	End in 2017	Flight with MS ALI
CHRIS-Proba	IS	VNIR	17–34 m	~6 d with 30° pointing	Operating	Multiangular capabilities
Landsat	MS	VSWIR & TIR	30 m	16 d	Operating	Long data record
Sentinel-2	MS	VSWIR	10–20 m	5 d	Operating	High spatio-temporal resolution
Sentinel-3	MS	VNIR & TIR	300 m	1 d	Operating	Focus on ocean monitoring
ASTER	MS	VSWIR & TIR	15–30 m	16 d	Operating	Good SWIR sampling (until 2008)

119 review of single examples in the literature. Special attention is put on the assessment of synergies between  
 120 spacebased IS and optical MS missions because of the open and large scale data availability expected for the  
 121 next years, thanks in particular to the co-existence of EnMAP, PRISMA, Sentinel-2 and Landsat missions.  
 122 Theoretical considerations and some examples of those synergies between IS and optical MS missions are  
 123 presented in Section 2. Potential synergies of IS with TIR and LiDAR measurements will be discussed in  
 124 Section 3. A summary of key points and a discussion of the implications of synergistic approaches for the  
 125 design and exploitation of future IS missions will be finally provided in Section 4.

## 126 2 Synergies of imaging spectroscopy with optical MS data

### 127 2.1 Approaches for synergistic use of optical IS and MS data

128 Synergies between spaceborne IS and optical MS measurements, e.g. from EnMAP/PRISMA and Sentinel-  
 129 2, respectively, could be developed in at least two different directions:

- 130 – Enhancement of the spatial resolution of the IS data through fusion with higher resolution MS data
- 131 – Improvement of mapping capabilities through the joint exploitation of MS and IS data sets

132 The fundamental basis for these two types of synergistic approaches and some examples are discussed  
 133 hereinafter in this section.

### 134 2.1.1 Enhancement of spatial resolution of IS data through fusion with MS data

135 Recently, considerable attention has been paid to the development of resolution enhancement techniques for  
136 IS imagery via IS and MS data fusion (Yokoya et al., 2017). The resolution enhancement of IS imagery can  
137 be performed by fusing a low-resolution IS image with a higher-resolution MS image, where both images  
138 are acquired over the same Earth's surface in the same season under similar atmospheric and illumination  
139 conditions. The resolution-enhanced IS data have the high spatial resolution of the MS sensor and the  
140 high spectral resolution of the IS sensor. Such high-order image products, which can be generated by  
141 using operational satellites (e.g., EnMAP and Sentinel-2), have the potential to enable a variety of new IS  
142 applications on a global scale, including high-resolution mapping of minerals, urban surface materials, and  
143 plant species.

144 The final goal for the sharpening of IS data would be the accurate reconstruction at high spatial resolu-  
145 tion of not only the broadband spectral shape, but also the single absorption features present in the spectrum.  
146 From a theoretical point of view, an absorption feature in the IS data can only be spatially-sharpened with  
147 higher resolution MS data if (and only if) the IS spectra represent pure spectra at the MS resolution, and at  
148 least one of the following conditions holds:

- 149 1. the absorption feature is wide enough to be sampled by the MS instrument (e.g. chlorophyll or iron, see  
150 Fig. 3a)
- 151 2. the material causing the absorption feature of interest also presents absorption features in other parts  
152 of the spectrum which are wide enough to be sampled by the MS instrument (e.g. liquid water presents  
153 absorption features with varying depth within the entire 950–2500 nm window, see Fig. 3b)
- 154 3. the material causing the absorption feature of interest tends to co-exist with other materials presenting  
155 absorption features in parts of the spectrum sampled by the MS instrument (e.g. chlorophyll and liquid  
156 water contents tend to covary in healthy vegetation)

157 The increase of information content of the spatially-enhanced IS data would depend on which of those  
158 three conditions applies. In the case of (1), the absorption feature is already sampled at high spatial res-  
159 olution in the MS data, but the spatially-enhanced IS data set would allow the application of band fitting  
160 retrieval algorithms, which can lead to more robust retrievals. Concerning (2), weaker absorption features  
161 can be spatially-enhanced through leverage with other parts of the spectrum at which the same material  
162 presents absorption features, the advantage of this being that the sharpened narrow features may be less  
163 affected by confounding factors than the wider ones sampled by the MS spectrum. As for (3), the spa-  
164 tial enhancement of absorption features would only map the statistical coexistence of different materials  
165 represented in the spectrum, and the resulting sharpened features would not represent actual changes in  
166 the surface composition or condition for those pixels in which the co-existence between the two materials  
167 deviates from the expectation.

168 To solve the IS and MS data fusion problem, researchers have proposed various methods in the last  
169 decade. The existing literature can be categorized into two groups. The first group of methods is based on  
170 pan-sharpening. Pan-sharpening is a technique that fuses low-resolution MS and higher-resolution panchro-  
171 matic images to create a high-resolution MS image. Since pan-sharpening can be regarded as a special case  
172 of IS and MS data fusion, significant effort has been devoted to extending and generalizing existing pan-  
173 sharpening techniques for IS and MS data fusion. Representative methods include component substitution  
174 (Chen et al., 2014), multiresolution analysis (Selva et al., 2015), and patch-wise sparse representation meth-  
175 ods (Grohnfeldt et al., 2013).

176 The second group of methods solves the problem through the analysis of the latent spectral character-  
177 istics of the observed scene based on a subspace spanned by a set of basis vectors or spectral signatures  
178 of underlying materials (so-called endmembers). This approach includes various methods based on matrix  
179 factorization (Yokoya et al., 2012), spectral unmixing (Lanaras et al., 2015), and Bayesian probability (Wei  
180 et al., 2015). For instance, unmixing-based methods reconstruct a high-resolution IS image by estimating

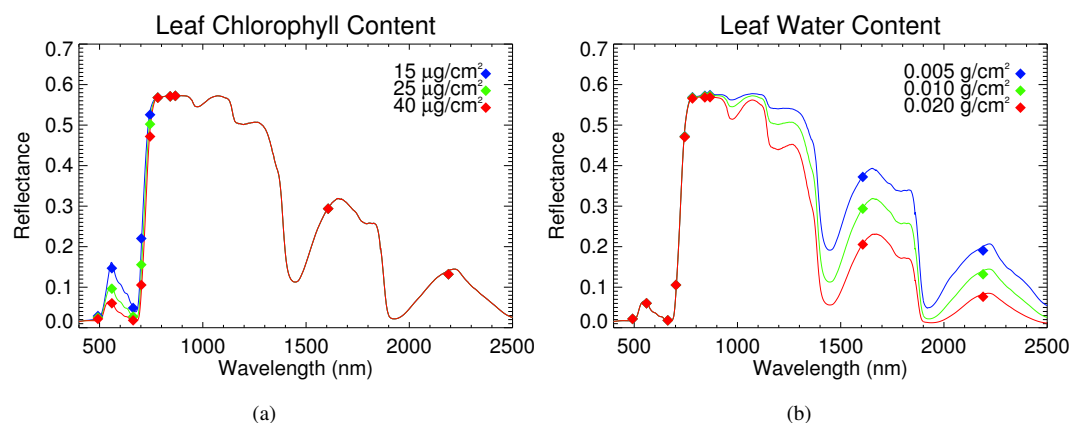


**Fig. 3** Top-of-canopy reflectance spectra at full spectral resolution and resampled to the 10–20 m channels of Sentinel-2 MSI for (a) different values of leaf chlorophyll content, and (b) different values of leaf water content.

181 spectral signatures of endmembers and high-resolution fractional abundances from the input IS and MS  
 182 images, respectively.

183 Methods above have been recently compared with extensive experiments in a review paper by Yokoya  
 184 et al. (2017). Multiresolution analysis based methods and unmixing based methods demonstrated good and  
 185 stable performance with different fusion scenarios. Current research on the development of algorithms for  
 186 IS and MS data fusion is focused on combining different approaches to further improve the reconstruction  
 187 performance.

188 Fig. 4 presents an example of IS and MS data fusion using simulated EnMAP and Sentinel-2 images  
 189 over an urban area of Brussels, Belgium. The fusion procedure is composed of two steps: 1) self-sharpening  
 190 of Sentinel-2 data that sharpens the 20-m-GSD bands by the 10-m-GSD bands, and 2) the fusion of En-  
 191 MAP and 10-m-GSD Sentinel-2 data. The multiresolution analysis based fusion technique presented in  
 192 Selva et al. (2015) was used for both steps. As shown in the color composite images in Fig. 4, the spatial  
 193 information content is significantly improved. On the other hand, the spectral profiles in Fig. 4 indicate that  
 194 the spectral quality is variable particularly in the SWIR range where the spectral coverage of Sentinel-2  
 195 is limited with only two bands. The importance of the overlap of spectral response functions between two  
 196 sensors is discussed in Yokoya et al. (2017).

197 Some publications have appeared in recent years reporting the impact of resolution enhancement of  
 198 IS imagery on spectral unmixing (Yokoya et al., 2016) and land-cover classification (Chan and Yokoya,  
 199 2016). Due to inevitable spectral distortions in the resolution-enhanced data, the use of external spectral  
 200 libraries does not always work for classification or spectral unmixing. In contrast, it has been shown that  
 201 good results can be obtained in classification or spectral unmixing by using reference spectra acquired from  
 202 each fused image (Yokoya et al., 2017, 2016).

203 Research on quality assessment of resolution-enhanced products is also important from a practical  
 204 viewpoint; however, very few publications can be found compared to those dealing with algorithm devel-  
 205 opment. Quantitative evaluation of resolution-enhanced data is usually performed within simulation studies  
 206 because reference data are necessary to quantify reconstruction performance. When resolution-enhanced IS  
 207 image products are generated from operational satellites (e.g., EnMAP and Sentinel-2), quantitative quality  
 208 assessment without reference is required to provide spectral quality at each pixel so that users can identify  
 209 and select reliable pixel spectra. The standard technique for this purpose is to examine consistency between  
 210 the input images and degraded versions of the fused image using quality measures (Palsson et al., 2016).



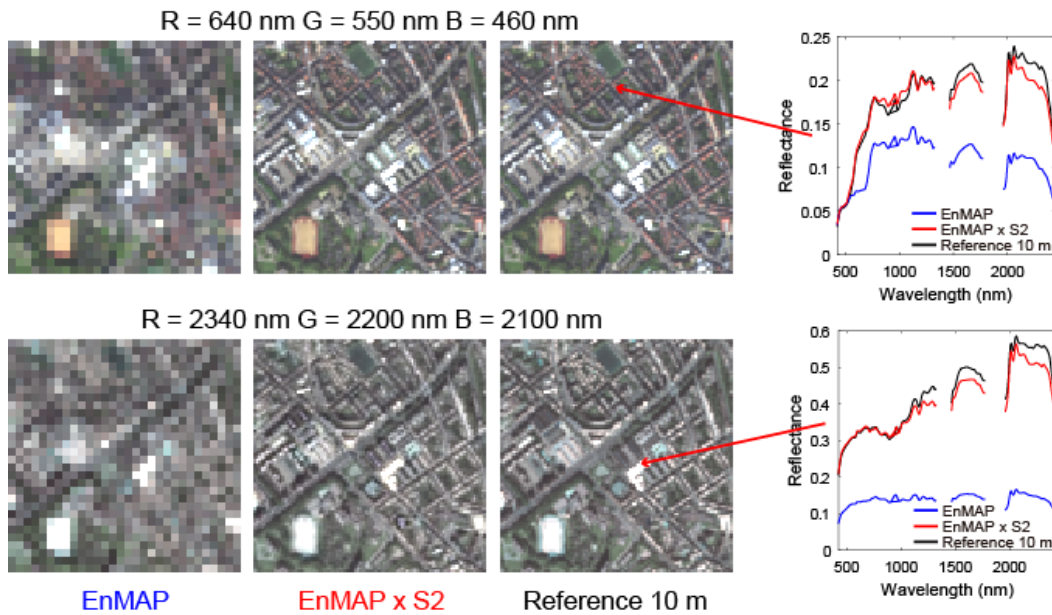


**Fig. 4** Example of spatial enhancement of IS data. Color composite images of simulated EnMAP, EnMAP-Sentinel-2 fused, and reference data over an urban area of Brussels (Belgium) are shown together with spectral signatures for two locations.

211 There is still room for investigation on how to integrate the consistency information obtained for each of  
 212 the two input images.

### 213 2.1.2 Improvement of mapping capabilities through the joint exploitation of MS and IS data sets

214 The high spectral resolution and coverage of IS instruments can also be used improved spatio-temporal  
 215 monitoring with MS data. This could be achieved through, at least, (i) analysis of IS results for the inter-  
 216 pretation of co-located MS measurements, and (ii) the extrapolation of IS-based information to the broad  
 217 spatial and temporal coverage of the MS data set.

218 *Analysis of IS results for the interpretation of MS measurements:* the richer spectral information in the IS  
 219 data complements the wider-area and higher spatio-temporal mapping capabilities of the MS instrument.  
 220 For example, Milewski et al. (2017) combined EO-1 Hyperion data with multitemporal and multispectral  
 221 Landsat acquisitions in order to analyze the spatial distribution of surface evaporite minerals and changes  
 222 in a Namibian Kalahari salt pan, which is a semi-arid depositional environment associated with episodic  
 223 flooding events. The dynamic of the surface crusts was evaluated through change detection analysis based  
 224 on a time series of Landsat acquisitions (1984–2015), whereas a hyperspectral image from Hyperion was  
 225 used to map the spatial distribution of the major crust types (halite, gypsum, calcite/sepiolite and disturbed,  
 226 dark crust) and their abundances through spectral mixture analysis (SMA). The combined information  
 227 from the hyperspectral and multispectral data sets could then be exploited to spatially differentiate and map  
 228 depositional environments over the whole salt pan.

229 In a different study, Mielke et al. (2014a) assessed the potential of combined IS and MS spaceborne  
 230 data for mapping the spatial extent of mine waste surfaces in South Africa. For that task, the broadband  
 231 iron feature depth (IFD) index was proposed as a potential proxy for mine waste. The IFD derived from  
 232 Landsat was found to be in good agreement with primary and secondary iron-bearing minerals mapped

233 from Hyperion data, which suggests that a combination of IS data for mineral identification with MS data  
234 for repetitive area-wide mapping of the IFD as a mine waste proxy is a promising synergistic application of  
235 IS and MS data. The use of the IFD index for geological applications based on combined IS and MS data  
236 will be further discussed in section 2.2.2.

237 Also dealing with geological mapping, Bishop et al. (2011) employed a two-step progressive approach,  
238 first to locate target areas characterized by hydrothermal mineral alteration using Advanced Spaceborne  
239 Thermal Emission and Reflection Radiometer (ASTER) VNIR and SWIR data, and secondly, to attempt  
240 detailed mineral mapping using Hyperion's spectral information.

241 *Extrapolation of IS-based information to the broad spatial and temporal coverage of the MS data:* In a  
242 different type of synergetic use of IS and MS data, the richer spectroscopic information delivered by the  
243 imaging spectrometer over a given area can be used to enhance the mapping potential of MS observations  
244 over a wider area than the one sampled by the IS data set.

245 For instance, Hubbard et al. (2003) combined Hyperion, EO-1 Advance Land Imager (ALI) and the  
246 co-orbiting ASTER data to map hydrothermally altered rocks associated with volcanic systems over the  
247 Central Andes. The mineral maps derived from Hyperion data with the Tetracorder expert system (Clark  
248 et al., 2003) were used to adjust image display thresholds in the alteration mineral maps derived from  
249 ALI and ASTER over a much broader area than the Hyperion coverage alone. Hyperion data were also  
250 used for the interpretation of ASTER and ALI mapping results as well as for their radiometric and atmo-  
251 spheric correction. A similar set-up was used by Hubbard and Crowley (2005) for mineral mapping over  
252 the Chilean-Bolivian Altiplano.

253 Schmid et al. (2005) used IS data to support the mapping of geophysical parameters in space and time  
254 with Landsat data. In particular, they developed an approach to monitor changes in wetlands in Central  
255 Spain. For this purpose, an SMA approach was used with a temporal series of Landsat data to detect changes  
256 in the wetland over time. The spectral endmembers for the SMA were extracted from hyperspectral data  
257 acquired during an airborne campaign, resampled to Landsat's TM and ETM+ spectral responses. It was  
258 used for change analysis at different and temporal scales, showing the feasibility of exploiting spectral  
259 endmembers derived from hyperspectral information in the analysis of MS data.

260 Concerning vegetation, optical MS measurements of vegetation reflectance spectra are generally sensi-  
261 tive to canopy water content (CWC), but quantitative estimates of CWC can only be reliably derived from  
262 IS radiance data through physical modeling of vapor and liquid water spectral features in the near-infrared.  
263 Asner et al. (2016) extrapolated CWC maps derived from airborne IS data over some sites to the entire  
264 state of California by means of a deep learning technique establishing empirical relationships between IS-  
265 based CWC and a series of parameters retrieved from Landsat and other ancillary data sets. The resulting  
266 California-wide CWC maps were analysed to assess the forest canopy water loss during the 2012–2015  
267 California drought.

268 *Model inversion and assimilation of multi-temporal data sets:* Strategies for the combination of IS and MS  
269 data can be based on a physical modeling of the geophysical parameters to be inferred from the remote  
270 sensing data, which complements the empirical approaches discussed in sections 2.1.1 and 2.1.2. Broadly  
271 speaking, this physical modeling means that the scene (e.g. land surface vegetation, atmosphere, ...) can  
272 be parameterized by a finite set of metrics (e.g. leaf area index, leaf pigment concentrations, soil optical  
273 properties, ...). These parameters can all be combined in a so-called *state vector*. Each observation, be it  
274 IS or MS, would provide an *inference* of the scene parameters: an uncertainty-quantified estimate of the  
275 state vector, or more precisely, the probability density function of the state vector. Parameters that can be  
276 inferred well because a particular observation has a strong sensitivity to it will be characterised by low  
277 uncertainty, whereas parameters with a large uncertainty will be symptomatic of low sensitivity in the  
278 observations. The mapping from observation to state vector is accomplished by inverting the observations

279 using an *observation operator*, typically a physical model based on radiative transfer theory that produces  
280 a prediction of the sensor observations as a function of the state vector.

281 In the case of multi-temporal data sets consisting of both MS and IS acquisitions, dynamic physically-  
282 based models allow us to blend in observations from the two sensors in a physically consistent manner. In its  
283 simplest form, we can imagine a scenario where MS and IS sensors fly over the same scene simultaneously.  
284 We can then invert the observations from one sensor, and use the inferred state vector probability density  
285 function as the *a priori* distribution of the second observation, which will result in a physically-based com-  
286 bination of both, respecting the characteristics of both sensors. The use of an observation operator allows  
287 one to account for different sensor characteristics (different illumination/viewing geometries, spectral sam-  
288 pling, spatial resolution, ...). The retrieval system is in this case combining two independent inferences of  
289 the same scene, acquired at the same time, to come to a solution that is consistent with both. An example  
290 will be discussed in Section 2.2.3.

291 If observations do not happen simultaneously, a first approach might be to assume that within a temporal  
292 window, the scene changes little, and thus they can be assumed simultaneous. However, this assumption  
293 can be broken in a few days for the land surface, and in less than an hour for atmospheric parameters.  
294 Dynamic models might be used to propagate the state vector at one location from one time step to another.  
295 The simplest possible dynamic model is to assume that nothing is changing, but to use this model under  
296 the assumption that it is wrong, and thus as model propagates the state over longer and longer time gaps  
297 will add uncertainty to the original estimate. This uncertainty inflation approach is the basis of temporal  
298 regularization e.g. (Lewis et al., 2012). More sophisticated approaches will use a dynamic model that  
299 describes the evolution of the state vector, but the concept of model uncertainty is still important, as even  
300 in the hypothetical case that the model was perfect, changes in the scene would render it wrong.

301 The approach described above has been widely used for dynamical systems, as well as climate studies,  
302 where it often is referred to as "data assimilation". A number of standard techniques, such as Kalman and  
303 particle filters, variational approaches, have been exploited to this end with Earth observation data. The  
304 same approaches can be used for IS and MS data combinations, provided that a reasonable observation  
305 operator is used. An example is shown in Fig 5, where we show the EO-LDAS system introduced in Lewis  
306 et al. (2012) being used to invert observations of surface directional reflectance from MS sensors, Landsat  
307 8 and Sentinel-2. In this experiment, Landsat 8 has fewer observations than Sentinel-2, so individual in-  
308 versions result in a very poor description of the dynamics of the parameter evolution over a year. It is also  
309 obvious that the single observations have large error bars, a consequence of the limited information con-  
310 tent on each observation. The situation improves with Sentinel-2, as the number of observations increases.  
311 However, the dynamics are not well described by this experiment: the clustering of observations results  
312 in an incomplete retrieval of the temporal evolution of the different parameters. Once we start applying a  
313 dynamic model, we get interpolation, but also reduced uncertainties, with both Sentinel-2 and Landsat 8  
314 being able to provide a reasonable path of the trajectory of the parameters. Once the dynamic model is es-  
315 tablished, it is straightforward to combine the observations from both sensors, resulting in a further reduced  
316 uncertainty.

## 317 2.2 Examples of synergistic use of IS and MS data

318 The theoretical discussion of potential synergies between optical IS and MS data presented in Section 2.1  
319 is complemented in this section with a series of examples of how such synergies work for selected study  
320 cases including land use and land cover mapping, mineral exploration, vegetation parameter retrieval and  
321 water applications.

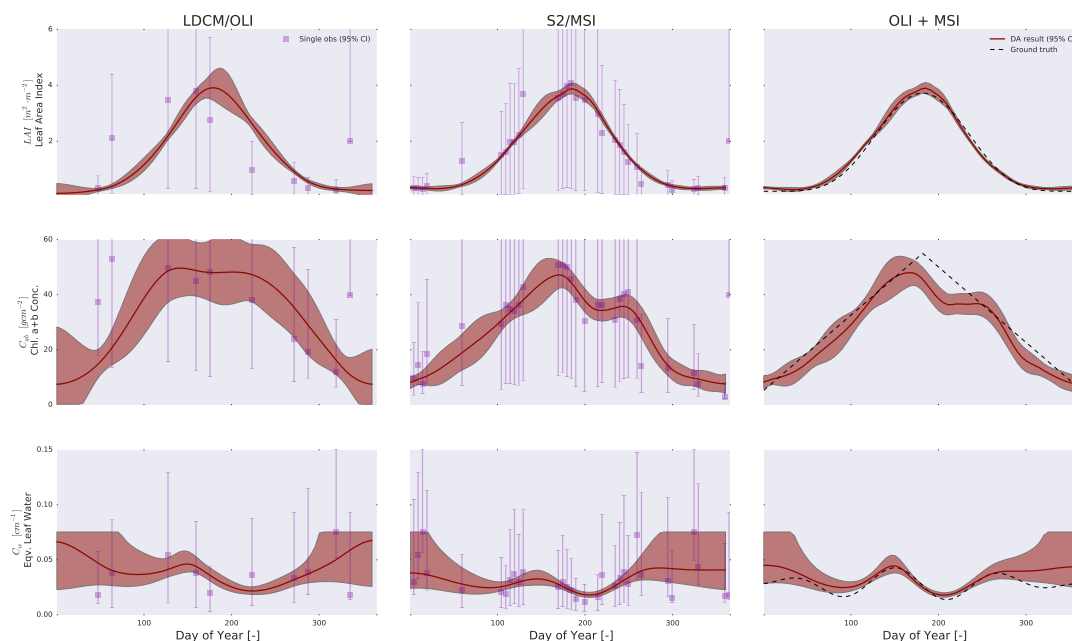


**Fig. 5** Synthetic experiment demonstrating "data assimilation" system to invert land surface parameters from MS observations. Here, we have simulated a scene where leaf chlorophyll  $C_{ab}$ , leaf area index  $LAI$  and equivalent leaf water  $C_w$  vary over time. The retrieved  $LAI$ ,  $C_{ab}$  and  $C_w$  are shown in each row (top to bottom, respectively). Each column shows the results of retrieving the parameters from Landsat 8 (left), Sentinel-2 MSI (center) and a combination of both. The dots with error bars refer to single observation inversions (mean and 1.96 times standard deviation), whereas the filled region shows the results of extending the inversions with a dynamic model and a variational data assimilation system.

### 322 2.2.1 Land use and land cover mapping

323 Land use and land cover (LULC) mapping is crucial to many scientific investigations from local to global  
 324 scales. For decades, land cover maps are used for urban planning and a multitude of environmental monitoring  
 325 applications such as urban expansion, forest inventory, biodiversity, land surface modeling, etc. LULC  
 326 mapping with satellite data is one of the most widely investigated subjects.

327 In the last two decades, extensive efforts have been devoted to understand IS data for LULC mapping.  
 328 However, airborne IS data are expensive and pose big processing challenges when coverage is very large,  
 329 whereas the typical 30 m GSD of spaceborne IS missions is in general too coarse for many applications.  
 330 To tackle this spatial issue, one possibility is to apply superresolution image reconstruction algorithms. Su-  
 331 perresolution enhanced hyperspectral VNIR CHRIS/Proba data (9 m) data have been tested for land cover  
 332 classification and unmixing (Chan et al., 2011). Demarchi et al. (2012) applied the same methodology for  
 333 subpixel mapping. The impression is that these superresolution enhanced data sets have not been satisfacto-  
 334 rily evaluated and hence their real potential remains uncertain. A major issue is the difficulty of compiling  
 335 such data set with reliable groundtruth. Another issue is the algorithm evaluation method: how should the  
 336 accuracy be evaluated for data sets acquired at different spatial resolution. Traditional accuracy measures  
 337 for land cover classification have long been criticized as limited and problematic (Foody, 2002).

338 Recent development in pan-sharpening techniques and image fusion and the highly anticipated new  
 339 spaceborne IS missions (e.g. EnMAP, HypIRI) have ignited new momentum in the spatial enhancement of  
 340 satellite IS images. While the issues related to an appropriate evaluation method still exist, one significant  
 341 obstacle has been overcome – there will be real accessible data sets, such as EnMAP and Sentinel-2. Many

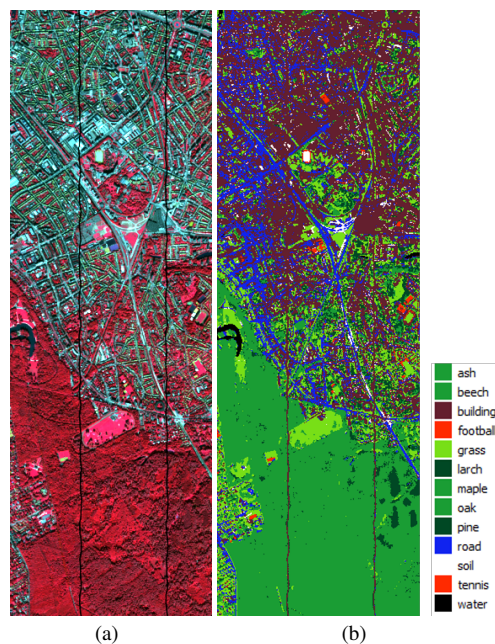


**Fig. 6** Land use and land cover mapping over Brussels. A false color composite of the study area from airborne APEX IS data is shown in (a), and a classification map using Canonical Correlation Forest (CCF) is depicted in (b).

342 methods fusing high resolution MS data and low-resolution IS data have been proposed targeting such  
 343 future data sets. However, real examples of applying a fused and spatially-enhanced IS image for LULC  
 344 classification are still comparatively rare.

345 To illustrate the usefulness of IS-MS fused images for LULC mapping, an APEX data set acquired  
 346 from the Brussels capital region has been used. It has 288 bands between 400–2500 nm and is acquired  
 347 at a GSD of 2.4 m (Chan and Yokoya, 2016). An EnMAP image with 242 bands is simulated with the  
 348 EnMAP end-to-end simulator tool (Segl et al., 2012) at a 30 m GSD to mimic low-resolution IS data. A  
 349 Sentinel-2 data set with 10 bands at 10 m and 20 m GSDs is also simulated using the S2eteS Sentinel-2  
 350 scene simulator (Segl et al., 2015). A generic 13-class land cover classification scheme is adapted for the  
 351 study area: larch, pines, ash, maple, oak, beech, grassland (cropland, lawn and parks), buildings, roads, soil  
 352 (bare soil, fallowed field, construction site), tennis court, football field, and water surface (artificial lake and  
 353 canal). Fig. 6 shows the false color composite of the study area.

354 We compared the classification accuracy of EnMAP (30 m), Sentinel-2 (10 m and 20 m) and fused IS  
 355 image at 10 m. The fusion approach has been described in Section 2.1.1. A groundtruth IS image at 10 m  
 356 with the same spectral configuration as EnMAP is also simulated. All datasets are upscaled at 10 m with the  
 357 same number of rows and columns for comparison. A total of 1095 pixels are blind-tested for accuracy. Two  
 358 advanced classification algorithms, Rotation Forest (RF) (Rodriguez et al., 2006) and Canonical Correlation  
 359 Forest (CCF) (Rainforth and Wood, 2015), are investigated. Fig. 6b shows the classification map generated  
 360 from an IS image at 10 m resolution which is used as the benchmark for comparison; a legend with only 8  
 361 colors is used for easy visualization. Table 2 shows the overall accuracy, average class accuracy and kappa  
 362 values of the classification results. In general, CCF performs better than RF. The benchmark 10 m IS data  
 363 has achieved 70-74% (RF-CCF) overall accuracy. With Sentinel-2, the overall accuracy is 66-72%. With  
 364 EnMAP at 30 m, the O.A. is 61-67%. For the fused IS data set, accuracies are 68%-73%. The performance

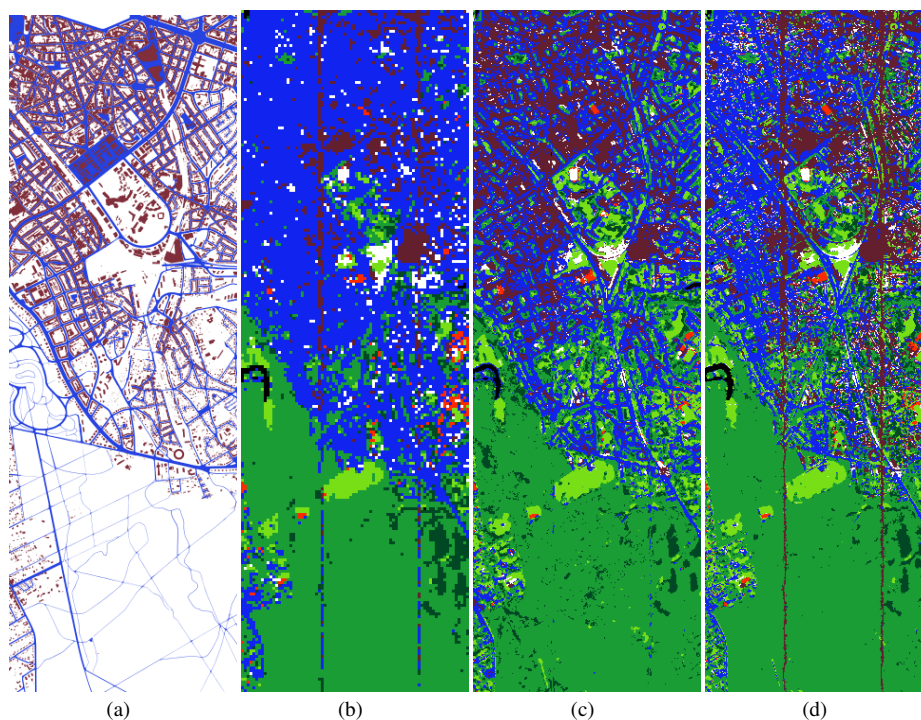


**Fig. 7** Ground-truth map of road and building classes (a) and classification results for EnMAP (b), Sentinel-2 (c) and fused image (d).

365 of the enhanced data is a little lower than the benchmark IS, moderately higher than the Sentinel-2, but  
366 significantly (5%) better than the 30 m EnMAP.

367 Fig. 7 clearly shows that the fused IS image reveals important details such as road networks compar-  
368 able to Sentinel-2 but at a higher accuracy. Extraction and classification of urban objects such as road  
369 and buildings are understandably too challenging with EnMAP at 30 m resolution. This explains the high perfor-  
370 mance of Sentinel-2. Comparison between MS and IS for land cover classification have been widely studied  
371 and depending on the application; IS imagery does not always have superior performance (Xu and Gong,  
372 2007). A MS-IS fusion approach is more suitable for challenging problems that require very rich spectral  
373 information and are better addressed with IS data. Our example shows that fusion of high-resolution MS  
374 and low-resolution IS images can achieve synergies in terms of significant improvement in classification  
375 details as compared with the low-resolution data and higher class accuracies as compared to the MS data.  
376 We expect the fusion synergies to have a significantly greater impact on specific LULC applications which  
377 require spatial details to characterize range, combination, distribution and clustering of species. For exam-  
378 ples, urban mapping (Herold et al., 2004), vegetation species mapping (Chan and Paelinckx, 2008), and  
379 biodiversity information required for environmental assessments (Bush et al., 2017). Given the fact that  
380 spaceborne IS data at 30 m GSD will only be available in the next few years, the novelty of a potential  
381 fused IS data at high GSD (10 m) with large coverage is almost certain to attract new research momentum  
382 with innovative LULC applications.

**Table 2** Comparison of classification accuracies with 13 classes. The highest accuracy is found for the reference data set, and the second highest for the fused data set. OA stands for overall accuracy and AA for average accuracy.

Classifier	Rotation Forests			Canonical Correlation Forests		
	OA	AA	Kappa	OA	AA	Kappa
Reference	69.11	75.87	0.63	74.45	72.73	0.70
EnMAP	61.98	62.80	0.56	67.63	66.11	0.62
Sentinel-2	66.85	62.78	0.61	72.70	70.73	0.68
Fused	68.02	73.04	0.63	73.94	72.38	0.69

### 383 2.2.2 Mineral mapping

384 The Haib River Cu-Mo deposit in the lower Orange river region represents a unique test site for the demon-  
385 stration of synergistic applications in geological remote sensing. Using simulations from HyMAP data,  
386 Mielke et al. (2014a) showed that it is possible to link data from state of the art MS systems such as  
387 Sentinel-2 and Landsat-8 to results from hyperspectral systems such as EnMAP via the IFD iron index  
388 introduced in Section 2.1.2. This absorption in the 900 nm region is caused by iron bearing minerals that  
389 may be produced by the weathering of metal sulfides such as pyrite and chalcopyrite (Chavez Jr., 2000).  
390 This process forms gossan surfaces that may be targeted with e.g. Sentinel-2, calculating the Normalized  
391 Iron Feature Depth from Sentinel-2 L1C data as shown in Fig. 8. The IFD is a simple three-point band  
392 depth index for MS sensor systems that proxies the band-depth of the iron feature near 900 nm using the  
393 two spectral bands which are closest to the shoulders of the 900 nm iron absorption feature (Mielke et al.,  
394 2014a). These two shoulder bands encompass the absorption band, which is closest to the 900 nm iron ab-  
395 sorption feature (Mielke et al., 2014a). The feature depth is found by an interpolation of the aforementioned  
396 iron absorption feature band with the shoulder bands. The difference between interpolated and measured  
397 iron feature absorption band yields the IFD (Mielke et al., 2014b). This may be used in mineral exploration  
398 to highlight gossan zones that may indicate the presence of sulphide ore deposits (Taylor, 2011). If this  
399 concept is expanded to other sensors, for example ASTER SWIR measurements, it is possible to derive a  
400 false color composite of the normalized feature depths, which highlight the dominant material mixture at a  
401 specific location, shown for the Haib River area in Fig. 8b.

402 However, hyperspectral data from spaceborne sensors such as EnMAP or PRISMA are necessary for  
403 a more detailed mineral mapping using e.g. expert systems such as the EnMAP Geologic Mapper (En-  
404 GeoMAP) Base, which is a fully automated system for the detection of mineralogical surface cover types  
405 over mineral deposit areas (Mielke et al., 2016). IS may be used for a detailed view on the local domi-  
406 nant minerals in one area, as shown in Fig. 9. Here the gossan zones, which have been identified in Fig. 8  
407 via the normalized iron feature depth may be subdivided into hematite, goethite and jarosite dominated  
408 gossans. Only IS data with its superior spectral resolution is able to correctly highlight and discriminate  
409 the most prominent minerals in the shortwave infrared from 2000 nm to 2500 nm. This shows the potential  
410 synergies in mineral exploration between large, multispectral, global mapping missions, such as Sentinel-2,  
411 and regional scale hyperspectral instruments such as EnMAP. The global mappers identify and highlight  
412 interesting anomalies for scientists working in mineral exploration, whilst IS data offers the capability to  
413 characterize these anomalies in much more detail using spectral geology tools such as EnGeoMAP for  
414 material identification.

### 415 2.2.3 Retrieval of vegetation parameters through model inversion

416 We can use the physical modeling introduced earlier to theoretically understand the limitations of different  
417 sensors for the retrieval of vegetation parameters, and how combining observations from different sensors  
418 might benefit parameter retrieval. To this end, we simulate a set of spectral acquisitions for EnMAP, as

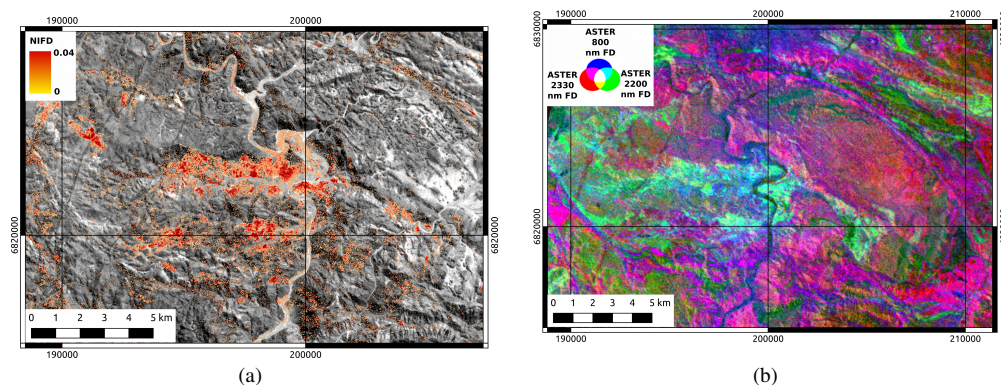


**Fig. 8** Indirect mapping of mineral types from multispectral remote sensing data over the Haib River Quartz Feldspar, Porphyry. The Sentinel-2 normalized iron feature depth data, which highlights the main ore bearing unit, appears as a large oval shaped anomaly in the central part of the image in (a). ASTER normalized feature depth composite image is shown in (b). It highlights mineral mixtures that are dominated by absorption features near 2330 nm (red), e.g. epidote, chlorite and carbonates. Illite, alunite and muscovite dominated areas are colored in green. Areas with material that shows prominent iron absorption features are colored blue.

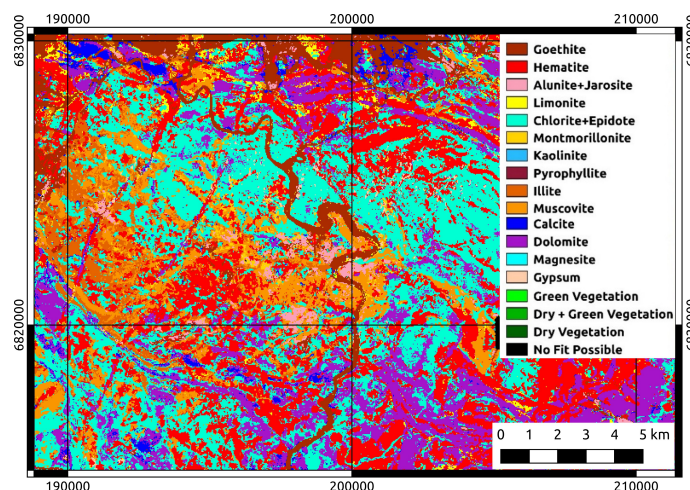


**Fig. 9** EnGeoMAP Base classification result from simulated EnMAP data. The areas dominated by chlorite, epidote and carbonates correspond well to the areas colored in magenta and red in Fig. 8b.

419 well as simultaneous observations from Sentinel-2/MSI. The simulations are done using the PROSPECT-  
 420 D leaf RT model (Féret et al., 2017) and the 4SAIL model (Verhoef, 1984) for leaf and canopy levels,  
 421 respectively. The atmospheric effects are simulated by the 6S model (Vermote et al., 1997), taking into  
 422 account the multiple interactions between land and atmosphere. The simulation thus presents a mapping  
 423 from surface and atmospheric composition parameters to at-sensor reflectances. With some indication of the  
 424 uncertainty in the observations at the sensor level, we can study the uncertainty of the retrieved parameters,  
 425 under the assumption that the "true state" of the combined surface and atmospheric system can be retrieved.  
 426 This uncertainty is encoded in the posterior covariance matrix, which we approximate by a linearization of



427 the Hessian as in Lewis et al. (2012). We consider an scenario where we have a thick vegetation canopy  
428 (high LAI), and a moderate atmospheric loading. We can see the uncertainty associated with the retrieval of  
429 different parameters in the left hand side column of Fig. 10, which depicts the posterior correlation matrix,  
430 where a perfect retrieval would be indicated by an identity matrix. We can see that for a single EnMAP  
431 observation, a substantial number of off-diagonal elements are present, suggesting parameters that result  
432 in changes to the measured reflectance in the same spectral window cannot be individually differentiated  
433 with a single observation. This is unsurprising, and that is the reason that many retrieval schemes prescribe  
434 some of these parameters (e.g. the leaf structure parameter  $N$ , the parameter(s) controlling the leaf angle  
435 distribution,  $ALA$ , or prescribing a soil response). The left hand side of Fig. 10 is in essence a depiction of  
436 the ill-posedness of the inversion problem. It is important to note that this example is contrived, as no prior  
437 information has been used at all, which would not be the case on any practical scenario.

438 On the right hand side panel of Fig. 10, we show the posterior correlation matrix where the EnMAP  
439 observations have been optimally combined with the information retrieved from a Sentinel-2/MSI obser-  
440 vation. We have assumed that these occur at different times, but close enough for the land surface to only  
441 have experienced a small change, but no extra information is gained on the atmospheric composition, and  
442 we have also ignored the 1375 nm band in Sentinel-2 MSI. It is clear that the posterior correlation matrices  
443 are much closer to a diagonal matrix, suggesting that some parameters such as leaf chlorophyll content,  
444 carotenoid content and anthocyanins might be well resolved. Other important parameters, such as LAI can  
445 be retrieved for high canopy cover, but the multiple scattering between the canopy and the atmosphere  
446 for low LAI results in a strong compensatory effect with aerosol optical thickness (AOT). Note that we  
447 cannot show the posterior covariance matrix for the Sentinel-2 MSI observation in this example: we are  
448 approximating the problem as a linear problem, in which we try to infer fourteen surface and atmosphere  
449 parameters, and with Sentinel-2 MSI we only have twelve bands, which results in an undetermined linear  
450 system.

451 Although in this example we have not assessed whether the solution can be found from the data, only  
452 what shape the uncertainty would take, the method used forms the basis of any Bayesian update, being  
453 the fundamental basis of techniques like Kalman or particle filters and smoothers (Gómez-Dans et al.,  
454 2016). Extended with a state vector dynamic model, the system would not only just provide inferences at  
455 the time of the acquisitions, but would also be able to optimally interpolate the state vector and provide  
456 uncertainty quantified inferences. The probabilistic basis of the Bayesian combination method rests on the  
457 two observations being interpreted by the same physical model with the same parameters, the assumption  
458 that the two sensors are accurately calibrated to a common standard, and that the different spatial resolutions  
459 can be bridged (by e.g. modeling the individual IFOV of the individual sensors). Provided these conditions  
460 are maintained, the method can be extended to other sensors.

#### 461 2.2.4 Monitoring of inland and coastal waters

462 Regular observations of physical and biogeochemical components in inland and coastal waters provide es-  
463 sential information in the form of maps of water quality, bottom properties and bathymetry as needed for  
464 science and resource management (e.g. Palmer et al., 2015; Olmanson et al., 2008; Dekker et al., 2011;  
465 Mouw et al., 2015; Tyler et al., 2016). Depending on the scale of observations, the developments in wa-  
466 ter quality and biophysical parameter retrieval algorithms are driven by airborne IS (e.g. AVIRIS, APEX),  
467 ocean colour (OC) radiometry (e.g. MODIS, MERIS) and MS sensors (e.g. Landsat, Sentinel-2). In par-  
468 ticular, the Sentinel-3/OLCI MS instrument offers an improve mapping potential for its specific capacities  
469 to resolve turbid, productive waters, and for having daily revisit with a 300 m GSD, whereas the Sentinel-  
470 2/MSI can provide data at a higher spatial resolution every 5 days. When combined with Landsat, a fine  
471 scale global mapping at a temporal resolution close to that of OC missions is also feasible. Finally, the pre-  
472 viously mentioned IS satellite missions (e.g. EnMAP, PRISMA, HypIRI) are anticipated to provide greatly  
473 enhanced capability to effectively enable wider applications for coastal and inland waters that, so far, have

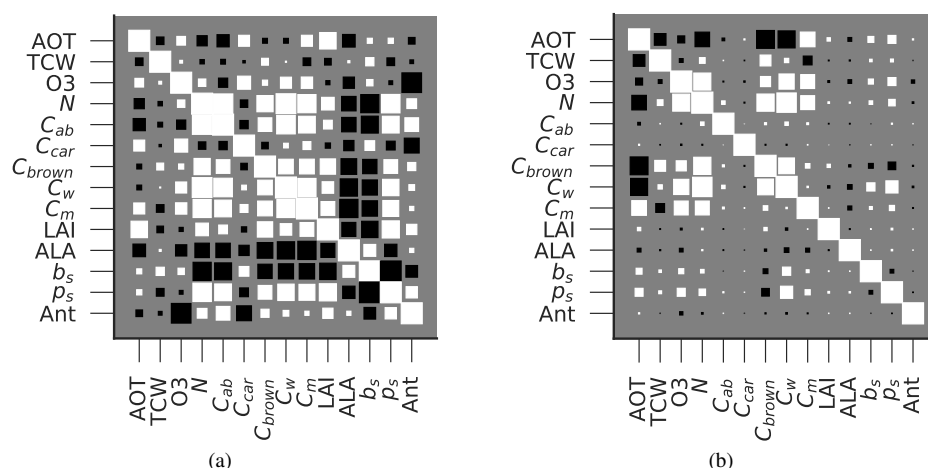


**Fig. 10** Posterior correlation matrices for the combined land and atmosphere RT models PROSAIL and 6S used to invert a single observation from the EnMAP sensor (a), and the equivalent matrices when the EnMAP observation is supplemented with a contemporary Sentinel2/MSI observation (b). The variables in the axis correspond to 6S and PROSAIL input parameters. The white (... black) squares indicate positive (... negative) correlation, and the size of the square is proportional to its absolute value. Elements along the main diagonal have a correlation of one.

474 been mostly based on Hyperion (e.g. Kutser, 2004), HICO (e.g. Garcia et al., 2014) and CHRIS-Proba (e.g.  
475 Casal et al., 2011).

476 IS data in fact allows both to increase the estimation accuracy of inland and coastal water variables  
477 currently observed by OC and MS sensors and to access to new variables of interest (e.g. identification and  
478 quantification of particulate and dissolved matter: type and size of suspended particles, types of pigments,  
479 organic matter composition, cyanobacteria) for multiple applications (Hestir et al., 2015; Giardino et al.,  
480 2018). In such a context, a prime example regards phytoplankton, a key parameter for water managers and  
481 of considerable interest to scientists who are for instance interested to freshwater ecology. As a proxy of  
482 phytoplankton biomass, the chlorophyll-a concentration (chl-a), was mapped in lakes already in 1974 from  
483 aircraft and satellite (Strong, 1974). It also represents a primary parameter quantitatively derived from OC  
484 (Mishra et al., 2017). Then, IS provides further insights for detecting the accessory pigments of phytoplank-  
485 ton such as phycocyanin and phycoerythrin pigments, which are often associated to harmful algal blooms.  
486 As an example, in occasion of a red ciliate blooms in coastal waters, Dierssen et al. (2015) used OC MODIS  
487 to map the chl-a concentration and IS HICO to further distinguish phycoerythrin pigments. An additional  
488 application in which IS provided enhanced mapping capability occurs in shallow waters, (those where the  
489 bottom is visible from the water surface and measurably influences the remote sensing reflectance). The  
490 patchy structure typical of these environments hinder the use of OC sensors so that monitoring of bottom  
491 types and benthic communities (e.g. mud, sand-mud mixture, coral sands, coral reefs, seagrass, macro-  
492 phytes) has been commonly achieved through MS sensors (e.g. Dekker et al., 2005). With a 10–30 m GSD,  
493 these sensors are ideal for most of the application scales, but are limited to identify species with similar  
494 spectral characteristics or to assess particular processes such as the state health of coral reefs (Botha et al.,  
495 2013). This is especially true for fine tracking of biodiversity and ecosystem functioning (identification  
496 of invasive and resident species). To this aim, airborne IS simultaneously providing high spatial and high  
497 spectral resolutions has been extensively used to make large-scale inventories of benthic photosynthetic  
498 organisms, such as macrophytes, seagrasses and corals (Phinn et al., 2008).

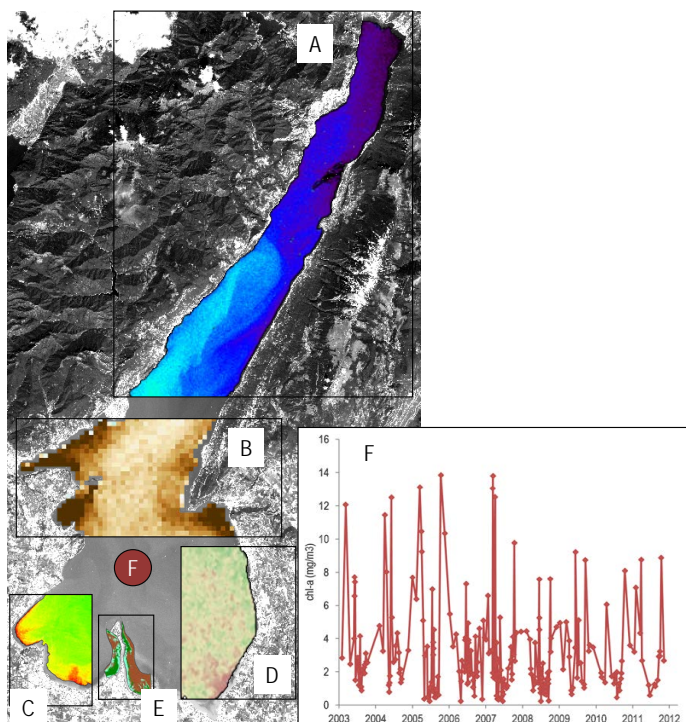


**Fig. 11** An overview of satellite products developed for Lake Garda. A: total suspended matter (SPM) to trace water dynamics from Sentinel-2 (17-08-2016, from blue to green the SPM ranges from 0.1 to 2 g/m<sup>3</sup>); B: coloured dissolved organic matter (CDOM) as a results of primary producers degradation from MERIS (11-10-2006, from light- to dark-brown CDOM ranges from 0.01 to 0.1 m<sup>-1</sup>); C: fine scale mapping of chlorophyll-a concentrations from Sentinel-2 (17-08-2016, from green to red chl-a ranges from 2 to 5 mg/m<sup>3</sup>); D: map of cyanobacterial bloom from HICO (23-08-2012, from green-yellow-red the cyanobacterial index, as a proxy of its biomass, increases); E: substrate type from airborne IS data (15-07-2005, in brown nude substrates, from cyan to light-green to dark-green: submerged vegetation beds with increasing vegetation density cover); F: time-series of chl-a from a pelagic station from MERIS.

499 To summarise, the optical complexity of inland and coastal waters, which also usually show a fast  
 500 degree of change and a patchy distribution of both water components and benthic habitats, make crucial  
 501 synergic applications of IS and MS. Moreover, dealing with water optics, the availability of OC sensors has  
 502 to be naturally included. As an example, we present the Lake Garda (Italy) test site, where at the beginning  
 503 of the nineties, Zilioli et al. (1994) started to study the lake colour from Landsat. The lake is characterised  
 504 by clear yet optically complex deep waters, with occasional cyanobacterial blooms and optically shallow  
 505 areas with important submerged macrophyte beds, which make it challenging to develop robust retrieval  
 506 algorithms. Nevertheless, the lake relevance (it is visited by more than 20 million tourists every year and  
 507 stores about 50 km<sup>3</sup> of water, used both for recreational purposes and water supply) is demanding a series  
 508 of applications that only synergistic use of IS, MS and OC are able to provide. Some of these applications  
 509 (e.g. the support to the EU Water Framework Directive to report on both chl-a concentration and extension

of submerged vegetation beds) are qualitatively shown in Fig. 11. For the sake of brevity we can only mention that most of these applications (namely A, B, C and E) were developed based on Hyperion data, that was used as a bench-mark for establishing a sensor-independent physically-based approach (Giardino et al., 2007). The use of HICO was instead useful to recognise the spectral feature due to the phycocyanin (Fig. 11D) according to Kutser (2004), while the neural network C2R operationally provided the MERIS-derived chl-a time series (Fig. 11E). A complete description of the applications can be found in Bresciani et al. (2011, 2012).

### 3 Potential synergies of IS with non-optical remote sensing data

#### 3.1 Synergies of IS with TIR data

TIR measurements hold a strong synergistic potential with optical data in general, and with IS in particular. The exploitation of synergies between VSWIR IS and multispectral TIR measurements is actually at the core of the NASA HypsIRI mission concept, which is intended to address a number of science questions focused on world ecosystems and natural hazards (Lee et al., 2015). HypsIRI is currently awaiting decision for implementation.

Based on the review by Lee et al. (2015), synergies between optical IS and multispectral TIR data can be important for, at least, the following applications:

- Canopy biochemistry: optical IS has demonstrated its potential to retrieve important leaf photosynthetic pigments, such as chlorophylls, carotenoids and anthocyanins, as well as leaf and canopy liquid water content (e.g. Ustin et al., 2004). This capability is well complemented by the ability of TIR measurements to measure other vegetation parameters such as cellulose, hemi-cellulose, cutin and other biochemicals with absorption features in the 8–14  $\mu\text{m}$  region (Ribeiro da Luz and Crowley, 2007).
- Plant functioning: simultaneous measurements of vegetation biophysical and biochemical properties and surface temperature can help monitor plant physiological functioning and potential stress situations as well as to estimate evapotranspiration (Anderson and Kustas, 2008), which is important to e.g. agricultural applications, water use practices and mitigation strategies in response to drought.
- Earth surface composition and change: the composition of exposed rock and soils can benefit from synergies between optical IS and TIR measurements, as the combination of spectral reflectance and emissivity measurements has been shown to be very helpful in identifying rocks, minerals and soils (e.g. Calvin et al., 2015; Eisele et al., 2015) which is of especial important for geological applications of remote sensing (van der Meer et al., 2012). This is due to the fact that the spectral features of e.g. silicates, clay minerals, iron oxides and hydroxides from the VSWIR and TIR range complement each other perfectly to material discrimination and quantification.
- Wildfires: optical IS and TIR measurements yield complementary capabilities to understand wildfire processes, and in particular the coupling between fires, vegetation and associated trace gas emissions. TIR measurements can be used to calculate fire radiative power and temperature, whereas spectroscopic measurements in the SWIR can be used to distinguish small hotter fires from large cooler fires (Matheson and Dennison, 2012) as well as to evaluate fire severity and vegetation recovery (Veraverbeke et al., 2012).
- Volcanoes: in addition to the capabilities of TIR remote sensing to monitor changes in temperature and gases indicating volcanic activity, the combination with optical IS measurements can help predict lava flows through the characterization of effusion rate and temperature.
- Urban environments: although limited by the high spatial resolution (<5 m) typically required by urban applications, the combination of optical IS and TIR has been shown to be very useful to characterize urban environments. The IS provides a high power of discrimination of manmade materials through

554 the different spectral signatures, whereas TIR measurements can be used to measure temperatures and  
555 characterize the associated urban heat island effect (Roberts et al., 2012).

556 In addition to HypsIRI, concurrent IS and TIR measurements will also be available from the ISS  
557 through the coordinated operation of ECOSTRESS and HISUI (Stavros et al., 2017). Such combined mea-  
558 surements can be used for a preliminary assessment of some of HypsIRI's scientific questions.

### 559 3.2 Synergies of IS with LiDAR data

560 LiDAR is an active remote sensing technology, using the time of flight of a laser pulse to compute a distance  
561 between the instrument and the backscattering (reflecting) object. With a precise estimate of the location  
562 and orientation of the measurement platform, a 3d coordinate of the reflecting object can be computed.  
563 LiDAR can be applied across a range of scales, from ground-based instruments to space-borne designs,  
564 serving very different purposes, as e.g. surveying forest stands (Danson et al., 2007) or measuring the  
565 decline of the polar ice-caps (Zwally et al., 2002). The most common LiDAR implementation, however, is  
566 in airborne laser scanners (ALS), where LiDARs are combined with a scanner to cover an across flight-track  
567 swath. Very high scanning frequencies (modern systems send several hundred thousand laser pulses per  
568 second) provide detailed 3d point clouds of the earth's surface. This 3d data is of largest benefit for surface  
569 types that have inherent 3d features, e.g. urban areas and forests. For the latter, IS suffers from structural  
570 effects (Hilker et al., 2008) and consequently, the fusion of ALS and IS has the largest potential for forested  
571 areas. So far, most studies were focused on airborne instruments, as there were only few spaceborne IS  
572 instruments and LiDARs, and the latter only in very large footprints not well suited for vegetation studies  
573 (e.g. ICESAT GLAS). The fusion of IS and ALS can be performed at various levels of the processing  
574 chain, but accurate co-registration of the data sets is key to all approaches. One of the straightforward  
575 ways of synergistic use of IS and ALS is to use the ALS derived digital surface model (DSM) to geo-  
576 locate the data of an IS system (typically push-broom sensors). Additional to the elevation model, more  
577 advanced approaches use both the IS and ALS intensity information in an overlapping wavelength domain  
578 (Fig. 12a) (Brell et al., 2016, 2017). This strategy enhances the synergistic use especially for the accurate  
579 co-registration of the two sensors (Brell et al., 2016).

580 In addition to the data level, fusion can as well be carried out at the product level, e.g. when combining  
581 two separate land-cover classifications based on separate IS and ALS data sets. Another aspect to classify  
582 fusion approaches is the choice of method. So far, most studies have used empirical frameworks for the fu-  
583 sion, e.g. a classifier or a regression model, but only few have used physical models of the radiative transfer  
584 to potentially improve results. A recent review of IS and ALS fusion approaches and their categorization by  
585 fusion level, approach and application can be found in Torabzadeh et al. (2014b). An important considera-  
586 tion is the notion of scale. IS and ALS data need to be similar in spatial extent and resolution for a genuine  
587 fusion of data sets. Larger mismatches in these two categories will result in methods being either up- or  
588 down-scaling or point-based cross-validation, e.g. in the case of a space-borne sampling LiDAR design  
589 (e.g. GEDI on the ISS) with a wall-to-wall IS instrument.

590 *Empirical Approaches:* Up to now, the majority of studies on IS and ALS fusion have used empirical  
591 approaches for land-cover classification (Torabzadeh et al., 2014b). In an early example, Koetz et al. (2008)  
592 fused IS and ALS data layers in a support vector machine framework to classify land-cover types including  
593 fuel-types in a wildland-urban interface to assess and mitigate forest fire risk. ALS and IS were highly  
594 complementary, having a much higher accuracy when combined, with the height information of ALS being  
595 particularly helpful for vegetation canopy height classes. Regarding tree species classification, accuracy for  
596 a temperate mixed forest comprising 8 species was increased from 75% when using either ALS or IS alone  
597 to 90% when combining the datasets (Torabzadeh et al., 2014a). Both ALS and IS features were aggregated

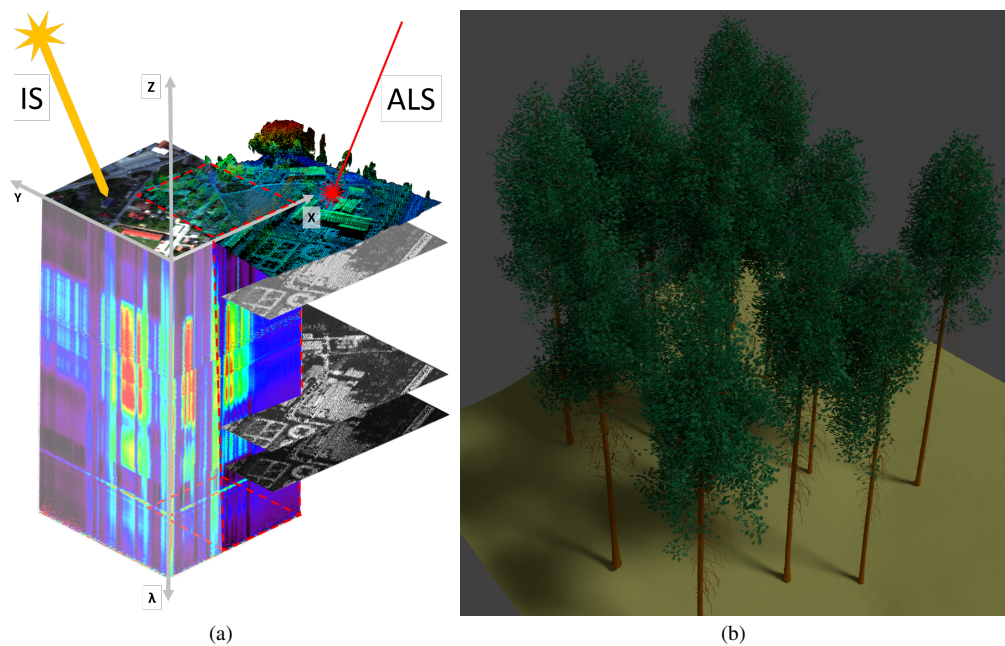


**Fig. 12** Combination of IS and LiDAR (airborne laser scanner, ALS) data. A schematic view of the combination is shown in (a), and a 3d model of a pine stand (Tharandt, Germany) reconstructed within the 3d vegetation laboratory project using laser scanning is displayed in (b). Laser scanning was at three different levels to model the pine stand: lab (for the shoot structure), ground (stems and branch structure) and airborne (tree locations and dimensions) (see Eysn et al. (2013) for details).

598 to individual tree crowns in this study. The high complementarity of ALS and IS for vegetation studies is  
 599 as well confirmed by the large-scale campaigns and results of the Carnegie Airborne Observatory, flying IS  
 600 and ALS sensors simultaneously, forming an ideal tool for 3d ecosystem assessment (Asner et al., 2012).

601 *Physical Approaches:* A potential tool to maximize the complementary exploitation of IS and ALS data are  
 602 radiative transfer models, which add a physical layer in understanding and exploiting the signals recorded  
 603 by both ALS and IS. A first of its kind, Koetz et al. (2007) used two different RTMs, one for IS, one  
 604 for LiDAR, in a fused look-up table inversion retrieval of biochemical and biophysical variables such as  
 605 LAI and fractional cover. However, results were mixed, likely hindered by the two models having distinct  
 606 physical realities and differing parameterizations. For increased understanding of IS signals over vegetation,  
 607 a possible solution is to derive an ALS based parameterization of the vegetation canopy, applied in an RTM  
 608 to forward simulate the spectral response. This was successfully done with the ESA STSE “3d Vegetation  
 609 Laboratory” - project (see Fig. 12b for an example 3d model) and such modeling tools will contribute to  
 610 better fusion approaches for future missions (Schneider et al., 2017).

611 Besides the modeling approaches, physically based synergies between inflight IS and ALS data are  
 612 being investigated. Based on radiative transfer modeling and ray-tracing approaches, the highly comple-  
 613 mentary sensor responses are physically adopted, and the active-passive dualism can be used to acquire  
 614 more reliable and comparable hyperspectral data (Brell et al., 2017). This intensity based cross-calibration  
 615 between the two sensors is a first physical based step to exploit active-passive synergies, with the specified  
 616 goal of combining structural and spectral information for a comprehensive surface object description.

617 *Level-0 fusion (multi-spectral LiDAR)*: The ultimate fusion of IS and ALS would be the development  
618 of a hyper-spectral LiDAR and implement that in an airborne design, remedying many issues of passive  
619 optical systems. However, up to now, only laboratory designs are truly hyperspectral due to their use a  
620 supercontinuum light source (Junttila et al., 2015), while the commercial ALS systems are multi-spectral  
621 only (3 wavelengths maximum in the Optech Titan system). In these implementations, however, not the  
622 small number of bands is the largest limitation, but the missing spatial and temporal synchronization of the  
623 wavelengths. This will lead to large errors for band ratios with only small signals (e.g. the photochemical  
624 reflectance index), as reflectance and structural differences are mixed between the different wavelengths.  
625 Only a design where all wavelengths sample exactly the same footprint (preferably at the same time) will  
626 provide accurate band ratios, which can be linked to foliage biochemistry (Morsdorf et al., 2009; Wood-  
627 house et al., 2011).

628 Technology and system characteristic of spaceborne LiDAR instruments differ significantly from air-  
629 borne systems. However, airborne based insights can be used for the development of synergies between  
630 various spectral and spatial sparse overlaps of spaceborne IS and LiDAR instruments. Upcoming systems  
631 like e.g. GEDI, ICESat-2 ATLAS (Abdalati et al., 2010) and the Methane Remote Sensing Lidar Mission  
632 (MERLIN) (Ehret et al., 2017) demonstrate the rapid advances in spaceborne LiDAR technology. This  
633 indicates that in the future, large footprints and the lack of spatial coverage will be overcome.

634 It must be stated that synergistic applications can also be found for the combination of IS with radar, al-  
635 though to a lesser extent than with LiDAR in part due to the non-overlapping wavelength domains. Demon-  
636 strated synergies between IS and radar are relatively similar to those between IS and LiDAR in the sense  
637 that radar provides the information on object structure to complete the spectral information from the IS  
638 image. Examples in the literature show the potential of synergies between IS and radar for the retrieval of  
639 vegetation properties (Treuhhaft et al., 2002), urban mapping and land use classification (Hu et al., 2017)  
640 and oil spill mapping (Dabbiru et al., 2015).

#### 641 **4 Summary and conclusions**

642 This contribution has discussed potential avenues for the synergistic use of IS and other sources of remote  
643 sensing data, with a focus on synergies with optical MS satellite missions because of their co-existence  
644 with spaceborne IS missions in the next years after the launch of EnMAP and PRISMA.

645 Optical IS and MS satellite missions can benefit from each other in two directions. On the one hand,  
646 IS acquisitions can be spatially-enhanced through fusion with higher spatial resolution MS data sets, as it  
647 would be the case of the combination of EnMAP and PRISMA with Sentinel-2 10–20 m GSD data. Such  
648 spatial sharpening of IS data has been shown to have a strong potential for LULC applications, and in  
649 especial for those dealing with urban environments. On the other hand, the spatio-temporal monitoring po-  
650 tential of wide-swath MS systems can be complemented by the rich spectral information in IS data. For  
651 example, IS data can be used to interpret and refine information retrieved from the MS data over a wider  
652 area through the addition of complementary information (e.g. for multi-sensor monitoring of the composi-  
653 tion of land surfaces and coastal and inland waters). The combination with IS data also allows to improve  
654 retrievals by MS systems through the extra spectral information provided by the IS data (e.g. endmembers  
655 derived from the IS data can be used as input for spectral unmixing techniques applied to the MS data). In  
656 the particular case of vegetation, for which relatively accurate physical radiative transfer models exist to  
657 link spectral reflectance with leaf and canopy parameters, model inversion and data assimilation techniques  
658 have a strong potential for parameter retrieval and the consistent merging of time series of MS and IS data.

659 Two other important aspects regarding optical IS and MS synergies have not been addressed in the  
660 text. First, the high spectral resolution and coverage of spaceborne IS instruments can be used to support  
661 calibration/validation activities of MS instruments in vicarious calibration exercises. Second, a wide range  
662 of optical MS missions with very high spatial resolution are being deployed by the private sector. These very

663 high spatial resolution data hold an even bigger potential for spatial enhancement of IS data than Sentinel-  
664 2. This is especially true for the Worldview-3 mission (DigitalGlobe Inc.) which includes several spectral  
665 channels in the SWIR which can be expected to substantially improve the fusion results with respect to  
666 Sentinel-2.

667 In addition to optical MS data, TIR data yield strong synergistic potential with optical IS data for  
668 a number of application domains including the monitoring of vegetation functioning, natural hazards and  
669 surface composition. Such a synergy of co-located IS-TIR observations is the basis of the HypIRI mission  
670 concept currently under development by NASA (Lee et al., 2015). The potential of merging IS and LiDAR  
671 data for the characterization of e.g. vegetation covers and urban objects has been proven by several studies  
672 based on airborne data. Synergies of IS with both TIR and LiDAR data can be further tested through  
673 the joint operation of the HISUI spectrometer, the GEDI LiDAR and the ECOSTRESS multispectral TIR  
674 instrument to co-exist onboard the ISS (Stavros et al., 2017). However, the exploitation of such data set  
675 will be restricted to particular scientific studies because of the limited temporal and spatial overlap of the  
676 four instruments. In this regard, only the combination of optical IS and MS data can be considered for  
677 regular application in the next years thanks to the availability of Sentinel-2, Landsat and at least EnMAP  
678 and PRISMA in the 2018–2020 time frame. The development of unsupervised algorithms for the automatic  
679 co-location and synergistic exploitation of the two sources of data, either through the spatial enhancement  
680 of the IS data or the improvement of information extraction from the MS, can thus be considered as an  
681 important field of research in the next years. If such combined IS-MS data exploitation could become  
682 quasi-operational, it might have an impact on the definition of future spaceborne IS missions, as some  
683 observational requirements for the most demanding applications (e.g. spatial resolution for urban mapping)  
684 could be relaxed under the assumption that synergies with existing MS missions could compensate for such  
685 relaxation.

## 686 Acknowledgments

687 This paper is an outcome of a workshop on requirements, capabilities and directions in spaceborne imag-  
688 ing spectroscopy held at the International Space Science Institute (ISSI) in Bern, Switzerland, in Novem-  
689 ber 2016. LG, KS, MB, and CM were partly funded by the EnMAP Scientific Preparation programme  
690 (FKZ:50EE1617).

## 691 References

- 692 Abdalati, W., Zwally, H. J., Bindschadler, R., Csatho, B., Farrell, S. L., Fricker, H. A., Harding, D., Kwok,  
693 R., Lefsky, M., Markus, T., Marshak, A., Neumann, T., Palm, S., Schutz, B., Smith, B., Spinhirne, J., and  
694 Webb, C. (2010). The icesat-2 laser altimetry mission. *Proceedings of the IEEE*, 98(5):735–751.
- 695 Anderson, M. and Kustas, W. (2008). Thermal remote sensing of drought and evapotranspiration. *Eos*,  
696 *Transactions American Geophysical Union*, 89(26):233–234.
- 697 Asner, G. P., Brodrick, P. G., Anderson, C. B., Vaughn, N., Knapp, D. E., and Martin, R. E. (2016). Pro-  
698 gressive forest canopy water loss during the 2012–2015 california drought. *Proceedings of the National*  
699 *Academy of Sciences*, 113(2):E249–E255.
- 700 Asner, G. P., Knapp, D. E., Boardman, J., Green, R. O., Kennedy-Bowdoin, T., Eastwood, M., Martin,  
701 R. E., Anderson, C., and Field, C. B. (2012). Carnegie Airborne Observatory-2: Increasing science data  
702 dimensionality via high-fidelity multi-sensor fusion. *Remote Sensing of Environment*, 124(Supplement  
703 C):454 – 465.



- 704 Barnsley, M. J., Settle, J. J., Cutter, M., Lobb, D., and Teston, F. (2004). The PROBA/CHRIS mission: a  
705 low-cost smallsat for hyperspectral, multi-angle, observations of the Earth surface and atmosphere. *IEEE*  
706 *Transactions on Geoscience and Remote Sensing*, 42:1512–1520.
- 707 Bishop, C. A., Liu, J. G., and Mason, P. J. (2011). Hyperspectral remote sensing for mineral exploration in  
708 pulang, yunnan province, china. *International Journal of Remote Sensing*, 32(9):2409–2426.
- 709 Botha, E. J., Brando, V. E., Anstee, J. M., Dekker, A. G., and Sagar, S. (2013). Increased spectral resolution  
710 enhances coral detection under varying water conditions. *Remote Sensing of Environment*, 131(Supple-  
711 ment C):247 – 261.
- 712 Brell, M., Rogass, C., Segl, K., Bookhagen, B., and Guanter, L. (2016). Improving sensor fusion: A para-  
713 metric method for the geometric coalignment of airborne hyperspectral and lidar data. *IEEE Transactions*  
714 *on Geoscience and Remote Sensing*, 54(6):3460–3474.
- 715 Brell, M., Segl, K., Guanter, L., and Bookhagen, B. (2017). Hyperspectral and lidar intensity data fusion:  
716 A framework for the rigorous correction of illumination, anisotropic effects, and cross calibration. *IEEE*  
717 *Transactions on Geoscience and Remote Sensing*, 55(5):2799–2810.
- 718 Bresciani, M., Bolpagni, R., Braga, F., Oggioni, A., and Giardino, C. (2012). Retrospective assessment of  
719 macrophytic communities in southern lake garda (italy) from in situ and mivis (multispectral infrared  
720 and visible imaging spectrometer) data. *Journal of Limnology*, 71(1):19.
- 721 Bresciani, M., Stroppiana, D., Odermatt, D., Morabito, G., and Giardino, C. (2011). Assessing remotely  
722 sensed chlorophyll-a for the implementation of the water framework directive in european perialpine  
723 lakes. *Science of The Total Environment*, 409(17):3083 – 3091.
- 724 Bush, A., Sollmann, R., Wilting, A., and et al. (2017). Connecting Earth Observation to High-Throughput  
725 Biodiversity Data. *NATURE ECOLOGY & EVOLUTION*, 1(0176).
- 726 Calvin, W. M., F. Littlefield, E., and Kratt, C. (2015). Remote sensing of geothermal-related minerals for  
727 resource exploration in nevada. 53:517–526.
- 728 Candela, L., Formaro, R., Guarini, R., Loizzo, R., Longo, F., and Varacalli, G. (2016). The prisma mission.  
729 In *2016 IEEE International Geoscience and Remote Sensing Symposium (IGARSS)*, pages 253–256.
- 730 Casal, G., Kutser, T., Domínguez-Gómez, J., Sánchez-Carnero, N., and Freire, J. (2011). Mapping benthic  
731 macroalgal communities in the coastal zone using chris-proba mode 2 images. *Estuarine, Coastal and*  
732 *Shelf Science*, 94(3):281 – 290.
- 733 Chan, J. C. W., Ma, J., de Voorde, T. V., and Canters, F. (2011). Preliminary results of superresolution-  
734 enhanced angular hyperspectral (chris/proba) images for land-cover classification. *IEEE Geoscience and*  
735 *Remote Sensing Letters*, 8(6):1011–1015.
- 736 Chan, J. C.-W. and Paelinckx, D. (2008). Evaluation of random forest and adaboost tree-based ensemble  
737 classification and spectral band selection for ecotope mapping using airborne hyperspectral imagery.  
738 *Remote Sensing of Environment*, 112(6):2999 – 3011.
- 739 Chan, J. C.-W. and Yokoya, N. (2016). Mapping land covers of brussels capital region using spatially  
740 enhanced hyperspectral images. In *WHISPERS 2016*, pages 1–5. IEEE Xplore.
- 741 Chavez Jr., W. (2000). Supergene oxidation of copper deposits: Zoning and distribution of copper oxide  
742 minerals. 41:9–21.
- 743 Chen, Z., Pu, H., Wang, B., and Jiang, G. M. (2014). Fusion of hyperspectral and multispectral images:  
744 A novel framework based on generalization of pan-sharpening methods. *IEEE Geoscience and Remote*  
745 *Sensing Letters*, 11(8):1418–1422.
- 746 Clark, R. N., Swayze, G. A., Livo, K. E., Kokaly, R. F., Sutley, S. J., Dalton, J. B., McDougal, R. R., and  
747 Gent, C. A. (2003). Imaging spectroscopy: Earth and planetary remote sensing with the usgs tetracorder  
748 and expert systems. *Journal of Geophysical Research: Planets*, 108(E12):n/a–n/a.
- 749 Dabbiru, L., Samiappan, S., Nobrega, R. A. A., Aanstoos, J. A., Younan, N. H., and Moorhead, R. J.  
750 (2015). Fusion of synthetic aperture radar and hyperspectral imagery to detect impacts of oil spill in gulf  
751 of mexico. In *2015 IEEE International Geoscience and Remote Sensing Symposium (IGARSS)*, pages  
752 1901–1904.

- 753 Danson, F. M., Hetherington, D., Morsdorf, F., Koetz, B., and Allgower, B. (2007). Forest canopy gap  
754 fraction from terrestrial laser scanning. *IEEE Geoscience and Remote Sensing Letters*, 4(1):157–160.
- 755 Dekker, A. G., Brando, V. E., and Anstee, J. M. (2005). Retrospective seagrass change detection in a  
756 shallow coastal tidal australian lake. *Remote Sensing of Environment*, 97(4):415 – 433.
- 757 Dekker, A. G., Phinn, S. R., Anstee, J., Bissett, P., Brando, V. E., Casey, B., Fearn, P., Hedley, J.,  
758 Klonowski, W., Lee, Z. P., Lynch, M., Lyons, M., Mobley, C., and Roelfsema, C. (2011). Intercom-  
759 parison of shallow water bathymetry, hydro-optics, and benthos mapping techniques in australian and  
760 caribbean coastal environments. *Limnology and Oceanography: Methods*, 9(9):396–425.
- 761 Demarchi, L., Chan, J. C.-W., Ma, J., and Canters, F. (2012). Mapping impervious surfaces from su-  
762 perresolution enhanced chris/proba imagery using multiple endmember unmixing. *ISPRS Journal of*  
763 *Photogrammetry and Remote Sensing*, 72(Supplement C):99 – 112.
- 764 Dierssen, H., Mcmanus, G., Chlus, A., Qiu, D., Gao, B.-C., and Lin, S. (2015). Space station image captures  
765 a red tide ciliate bloom at high spectral and spatial resolution. 112.
- 766 Drusch, M., Bello, U. D., Carlier, S., Colin, O., Fernandez, V., Gascon, F., Hoersch, B., Isola, C., Laberinti,  
767 P., Martimort, P., Meygret, A., Spoto, F., Sy, O., Marchese, F., and Bargellini, P. (2012). Sentinel-2:  
768 Esa’s optical high-resolution mission for {GMES} operational services. *Remote Sensing of Environment*,  
769 120(0):25 – 36.
- 770 Drusch, M., Moreno, J., Bello, U. D., Franco, R., Goulas, Y., Huth, A., Kraft, S., Middleton, E. M., Migli-  
771 etta, F., Mohammed, G., Nedbal, L., Rascher, U., Schüttemeyer, D., and Verhoef, W. (2017). The FLu-  
772 orescence EXplorer Mission Concept – ESA’s Earth Explorer 8. *IEEE Transactions on Geoscience and*  
773 *Remote Sensing*, 55(3):1273–1284.
- 774 Ehret, G., Bousquet, P., Pierangelo, C., Alpers, M., Millet, B., Abshire, J. B., Bovensmann, H., Burrows,  
775 J. P., Chevallier, F., Ciais, P., Crevoisier, C., Fix, A., Flamant, P., Frankenberg, C., Gibert, F., Heim,  
776 B., Heimann, M., Houweling, S., Hubberten, H. W., Jöckel, P., Law, K., Löw, A., Marshall, J., Agustí-  
777 Panareda, A., Payan, S., Prigent, C., Rairoux, P., Sachs, T., Scholze, M., and Wirth, M. (2017). Merlin:  
778 A french-german space lidar mission dedicated to atmospheric methane. *Remote Sensing*, 9(10).
- 779 Eisele, A., Chabrillat, S., Hecker, C., Hewson, R., Lau, I. C., Rogass, C., Segl, K., Cudahy, T. J., Udelhoven,  
780 T., Hostert, P., and Kaufmann, H. (2015). Advantages using the thermal infrared (tir) to detect and  
781 quantify semi-arid soil properties. *Remote Sensing of Environment*, 163(Supplement C):296 – 311.
- 782 Eysn, L., Pfeifer, N., Ressler, C., Hollaus, M., Graf, A., and Morsdorf, F. (2013). A practical approach for  
783 extracting tree models in forest environments based on equirectangular projections of terrestrial laser  
784 scans. *Remote Sensing*, 5(11):5424–5448.
- 785 Féret, J. B., Gitelson, A. A., Noble, S. D., and others (2017). PROSPECT-D: Towards modeling leaf optical  
786 properties through a complete lifecycle. *Remote sensing of environment*.
- 787 Foody, G. M. (2002). Status of land cover classification accuracy assessment. *Remote Sensing of Environ-*  
788 *ment*, 80(1):185 – 201.
- 789 García, R. A., Fearn, P. R., and McKinna, L. I. (2014). Detecting trend and seasonal changes in bathymetry  
790 derived from hico imagery: A case study of shark bay, western australia. *Remote Sensing of Environment*,  
791 147(Supplement C):186 – 205.
- 792 Giardino, C., Brando, V. E., Dekker, A. G., Strömbeck, N., and Candiani, G. (2007). Assessment of water  
793 quality in lake garda (italy) using hyperion. *Remote Sensing of Environment*, 109(2):183 – 195.
- 794 Giardino, C., Brando, V. E., Gege, P., Pinnel, N., Hochberg, E., Knaeps, E., Reusen, I., Doerffer, R., Bres-  
795 ciani, M., Braga, F., Foerster, S., Champollion, N., and Dekker, A. (2018). Imaging spectrometry of  
796 inland and coastal waters: State-of-the-art, achievements and perspectives. *Surveys in Geophysics*. in  
797 press.
- 798 Goetz, A. F. H., Vane, G., Salomon, J. E., and Rock, B. N. (1985). Imaging spectroscopy for Earth remote  
799 sensing. *Science*, 228:1147–1153.
- 800 Gómez-Dans, J., Lewis, P., and Disney, M. (2016). Efficient Emulation of Radiative Transfer Codes Using  
801 Gaussian Processes and Application to Land Surface Parameter Inferences. *Remote Sensing*, 8(2):119.

- 802 Green, R. O., Eastwood, M., Sarture, C., Chrien, T., Aronsson, M., Chippendale, B., Faust, J., Pavri, B.,  
803 Chovit, C., Solis, M., Olah, M., and Williams, O. (1998). Imaging spectroscopy and the airborne visi-  
804 ble/infrared imaging spectrometer (AVIRIS). *Remote Sensing of Environment*, 65:227–248.
- 805 Grohnfeldt, C., Zhu, X. X., and Bamler, R. (2013). Jointly sparse fusion of hyperspectral and multispectral  
806 imagery. In *2013 IEEE International Geoscience and Remote Sensing Symposium - IGARSS*, pages  
807 4090–4093.
- 808 Guanter, L., Kaufmann, H., Segl, K., Foerster, S., Rogass, C., Chabrillat, S., Kuester, T., Hollstein, A.,  
809 Rossner, G., Chlebek, C., Straif, C., Fischer, S., Schrader, S., Storch, T., Heiden, U., Mueller, A., Bach-  
810 mann, M., Mühle, H., Müller, R., Habermeyer, M., Ohndorf, A., Hill, J., Buddenbaum, H., Hostert, P.,  
811 van der Linden, S., Leitão, P. J., Rabe, A., Doerffer, R., Krasemann, H., Xi, H., Mauser, W., Hank, T.,  
812 Locherer, M., Rast, M., Staenz, K., and Sang, B. (2015). The enmap spaceborne imaging spectroscopy  
813 mission for earth observation. *Remote Sensing*, 7(7):8830–8857.
- 814 Herold, M., Roberts, D. A., Gardner, M. E., and Dennison, P. E. (2004). Spectrometry for urban area  
815 remote sensing—development and analysis of a spectral library from 350 to 2400 nm. *Remote Sensing*  
816 *of Environment*, 91(3):304 – 319.
- 817 Hestir, E. L., Brando, V. E., Bresciani, M., Giardino, C., Matta, E., Villa, P., and Dekker, A. G. (2015).  
818 Measuring freshwater aquatic ecosystems: The need for a hyperspectral global mapping satellite mission.  
819 *Remote Sensing of Environment*, 167(Supplement C):181 – 195. Special Issue on the Hyperspectral  
820 Infrared Imager (HyspIRI).
- 821 Hilker, T., Coops, N. C., Hall, F. G., Black, T. A., Wulder, M. A., Nesic, Z., and Krishnan, P. (2008).  
822 Separating physiologically and directionally induced changes in pri using brdf models. *Remote Sensing*  
823 *of Environment*, 112(6):2777 – 2788.
- 824 Hu, J., Mou, L., Schmitt, A., and Zhu, X. X. (2017). Fusionet: A two-stream convolutional neural network  
825 for urban scene classification using polsar and hyperspectral data. In *2017 Joint Urban Remote Sensing*  
826 *Event (JURSE)*, pages 1–4.
- 827 Hubbard, B. and Crowley, J. K. (2005). Mineral mapping on the chilean–bolivian altiplano using co-orbital  
828 ali, aster and hyperion imagery: Data dimensionality issues and solutions. 99:173–186.
- 829 Hubbard, B. E., Crowley, J. K., and Zimelman, D. R. (2003). Comparative alteration mineral mapping  
830 using visible to shortwave infrared (0.4–2.4  $\mu\text{m}$ ) hyperion, ali, and aster imagery. *IEEE Transactions*  
831 *on Geoscience and Remote Sensing*, 41(6):1401–1410.
- 832 Junttila, S., Kaasalainen, S., Vastaranta, M., Hakala, T., Nevalainen, O., and Holopainen, M. (2015). Inves-  
833 tigating bi-temporal hyperspectral lidar measurements from declined trees—experiences from laboratory  
834 test. *Remote Sensing*, 7(10):13863–13877.
- 835 Koetz, B., Morsdorf, F., van der Linden, S., Curt, T., and Allgöwer, B. (2008). Multi-source land cover clas-  
836 sification for forest fire management based on imaging spectrometry and lidar data. *Forest Ecology and*  
837 *Management*, 256(3):263 – 271. Impacts of forest ecosystem management on greenhouse gas budgets.
- 838 Koetz, B., Sun, G., Morsdorf, F., Ranson, K., Kneubühler, M., Itten, K., and Allgöwer, B. (2007). Fu-  
839 sion of imaging spectrometer and lidar data over combined radiative transfer models for forest canopy  
840 characterization. *Remote Sensing of Environment*, 106(4):449 – 459.
- 841 Kutser, T. (2004). Quantitative detection of chlorophyll in cyanobacterial blooms by satellite remote sens-  
842 ing. *Limnology and Oceanography*, 49(6):2179–2189.
- 843 Lanaras, C., Baltasvias, E., and Schindler, K. (2015). Hyperspectral super-resolution by coupled spectral  
844 unmixing. In *The IEEE International Conference on Computer Vision (ICCV)*.
- 845 Lee, C. M., Cable, M. L., Hook, S. J., Green, R. O., Ustin, S. L., Mandl, D. J., and Middleton, E. M. (2015).  
846 An introduction to the nasa hyperspectral infrared imager (hyspirci) mission and preparatory activities.  
847 *Remote Sensing of Environment*, 167(Supplement C):6 – 19. Special Issue on the Hyperspectral Infrared  
848 Imager (HyspIRI).
- 849 Lewis, P., Gómez-Dans, J., Kaminski, T., Settle, J., Quaife, T., Gobron, N., Styles, J., and Berger, M. (2012).  
850 An Earth Observation Land Data Assimilation System (EO-LDAS). *Remote sensing of environment*,

- 120(0):219–235.
- 851 Lucke, R. L., Corson, M., McGlothlin, N. R., Butcher, S. D., Wood, D. L., Korwan, D. R., Li, R. R., Snyder,  
852 W. A., Davis, C. O., and Chen, D. T. (2011). Hyperspectral Imager for the Coastal Ocean: instrument  
853 description and first images. *Applied Optics*, 50(11):1501–1516.
- 854 Matheson, D. S. and Dennison, P. E. (2012). Evaluating the effects of spatial resolution on hyperspectral  
855 fire detection and temperature retrieval. *Remote Sensing of Environment*, 124(Supplement C):780 – 792.
- 856 Mielke, C., Boesche, N. K., Rogass, C., Kaufmann, H., Gauert, C., and de Wit, M. (2014a). Spaceborne  
857 Mine Waste Mineralogy Monitoring in South Africa, Applications for Modern Push-Broom Missions:  
858 Hyperion/OLI and EnMAP/Sentinel-2. *Remote Sensing*, 6(8):6790–6816.
- 859 Mielke, C., K. Boesche, N., Rogaß, C., Segl, K., Gauert, C., and Kaufmann, H. (2014b). Potential applica-  
860 tions of the Sentinel-2 multispectral sensor and the EnMAP hyperspectral sensor in mineral exploration.  
861 In *EARSeL eProceedings*, volume 13, page 93.
- 862 Mielke, C., Rogass, C., Boesche, N., Segl, K., and Altenberger, U. (2016). EnGeoMAP 2.0 – Automated  
863 Hyperspectral Mineral Identification for the German EnMAP Space Mission. *Remote Sensing*, 8(2).
- 864 Milewski, R., Chabrilat, S., and Behling, R. (2017). Analyses of recent sediment surface dynamic of a  
865 namibian kalahari salt pan based on multitemporal landsat and hyperspectral hyperion data. *Remote*  
866 *Sensing*, 9(2).
- 867 Mishra, D., Ogashawara, I., and Gitelson, A. (2017). In *Bio-optical Modeling and Remote Sensing of Inland*  
868 *Waters*, page 332. Elsevier.
- 869 Morsdorf, F., Nichol, C., Malthus, T., and Woodhouse, I. H. (2009). Assessing forest structural and physi-  
870 ological information content of multi-spectral lidar waveforms by radiative transfer modelling. *Remote*  
871 *Sensing of Environment*, 113(10):2152 – 2163.
- 872 Mouw, C. B., Greb, S., Aurin, D., DiGiacomo, P. M., Lee, Z., Twardowski, M., Binding, C., Hu, C., Ma,  
873 R., Moore, T., Moses, W., and Craig, S. E. (2015). Aquatic color radiometry remote sensing of coastal  
874 and inland waters: Challenges and recommendations for future satellite missions. *Remote Sensing of*  
875 *Environment*, 160(Supplement C):15 – 30.
- 876 Olmanson, L. G., Bauer, M. E., and Brezonik, P. L. (2008). A 20-year landsat water clarity census of min-  
877 nesota’s 10,000 lakes. *Remote Sensing of Environment*, 112(11):4086 – 4097. Applications of Remote  
878 Sensing to Monitoring Freshwater and Estuarine Systems.
- 879 Palmer, S. C., Kutser, T., and Hunter, P. D. (2015). Remote sensing of inland waters: Challenges, progress  
880 and future directions. *Remote Sensing of Environment*, 157(Supplement C):1 – 8. Special Issue: Remote  
881 Sensing of Inland Waters.
- 882 Palsson, F., Sveinsson, J. R., Ulfarsson, M. O., and Benediktsson, J. A. (2016). Quantitative quality eval-  
883 uation of pansharpened imagery: Consistency versus synthesis. *IEEE Transactions on Geoscience and*  
884 *Remote Sensing*, 54(3):1247–1259.
- 885 Phinn, S., Roelfsema, C., Dekker, A., Brando, V., and Anstee, J. (2008). Mapping seagrass species, cover  
886 and biomass in shallow waters: An assessment of satellite multi-spectral and airborne hyper-spectral  
887 imaging systems in moreton bay (australia). *Remote Sensing of Environment*, 112(8):3413 – 3425. Earth  
888 Observations for Marine and Coastal Biodiversity and Ecosystems Special Issue.
- 889 Rainforth, T. and Wood, F. (2015). Canonical Correlation Forests. *ArXiv e-prints*.
- 890 Ribeiro da Luz, B. and Crowley, J. K. (2007). Spectral reflectance and emissivity features of broad leaf  
891 plants: Prospects for remote sensing in the thermal infrared (8.0–14.0  $\mu\text{m}$ ). *Remote Sensing of Environ-*  
892 *ment*, 109(4):393 – 405.
- 893 Roberts, D. A., Quattrochi, D. A., Hulley, G. C., Hook, S. J., and Green, R. O. (2012). Synergies between  
894 vswir and tir data for the urban environment: An evaluation of the potential for the hyperspectral infrared  
895 imager (hypisiri) decadal survey mission. *Remote Sensing of Environment*, 117(Supplement C):83 – 101.  
896 Remote Sensing of Urban Environments.
- 897 Rodriguez, J. J., Kuncheva, L. I., and Alonso, C. J. (2006). Rotation forest: A new classifier ensemble  
898 method. *IEEE Transactions on Pattern Analysis and Machine Intelligence*, 28(10):1619–1630.
- 899

- 900 Roy, D., Wulder, M., Loveland, T., C.E., W., Allen, R., Anderson, M., Helder, D., Irons, J., Johnson, D.,  
901 Kennedy, R., Scambos, T., Schaaf, C., Schott, J., Sheng, Y., Vermote, E., Belward, A., Bindschadler, R.,  
902 Cohen, W., Gao, F., Hipple, J., Hostert, P., Huntington, J., Justice, C., Kilic, A., Kovalskyy, V., Lee, Z.,  
903 Lyburner, L., Masek, J., McCorkel, J., Shuai, Y., Trezza, R., Vogelmann, J., Wynne, R., and Zhu, Z.  
904 (2014). Landsat-8: Science and product vision for terrestrial global change research. *Remote Sensing of*  
905 *Environment*, 145(0):154 – 172.
- 906 Schmid, T., Koch, M., and Gumuzzio, J. (2005). Multisensor approach to determine changes of wetland  
907 characteristics in semiarid environments (central Spain). *IEEE Transactions on Geoscience and Remote*  
908 *Sensing*, 43(11):2516–2525.
- 909 Schneider, F. D., Morsdorf, F., Schmid, B., Petchey, O. L., Hueni, A., Schimel, D. S., and Schaepman,  
910 M. E. (2017). Mapping functional diversity from remotely sensed morphological and physiological  
911 forest traits. *Nature Communications*.
- 912 Segl, K., Guanter, L., Gascon, F., Kuester, T., Rogass, C., and Mielke, C. (2015). S2etes: An end-to-end  
913 modeling tool for the simulation of sentinel-2 image products. *IEEE Transactions on Geoscience and*  
914 *Remote Sensing*, 53(10):5560–5571.
- 915 Segl, K., Guanter, L., Rogass, C., Kuester, T., Roessner, S., Kaufmann, H., Sang, B., Mogulsky, V., and  
916 Hofer, S. (2012). Eetes - the enmap end-to-end simulation tool. *IEEE Journal of Selected Topics in*  
917 *Applied Earth Observations and Remote Sensing*, 5(2):522–530.
- 918 Selva, M., Aiazzi, B., Butera, F., Chiarantini, L., and Baronti, S. (2015). Hyper-sharpening: A first approach  
919 on sim-ga data. *IEEE Journal of Selected Topics in Applied Earth Observations and Remote Sensing*,  
920 8(6):3008–3024.
- 921 Stavros, E. N., Schimel, D., Pavlick, R., Serbin, S., Swann, A., Duncanson, L., Fisher, J. B., Fassnacht, F.,  
922 Ustin, S., Dubayah, R., Schweiger, A., and Wennberg, P. (2017). ISS observations offer insights into  
923 plant function. *Nature Ecology & Evolution*, 1(0194).
- 924 Strong, A. E. (1974). Remote sensing of algal blooms by aircraft and satellite in lake Erie and Utah Lake.  
925 *Remote Sensing of Environment*, 3(2):99 – 107.
- 926 Taylor, R. (2011). In *Gossans and Leached Cappings – Field Assessment*, page 146. Springer, Berlin-  
927 Heidelberg.
- 928 Thompson, D. R., Boardman, J. W., Eastwood, M. L., and Green, R. O. (2017). A large airborne survey of  
929 earth's visible-infrared spectral dimensionality. *Opt. Express*, 25(8):9186–9195.
- 930 Torabzadeh, H., Morsdorf, F., Leiterer, R., and Schaepman, M. (2014a). Fusing imaging spectrometry  
931 and airborne laser scanning data for tree species discrimination. In *Geoscience and Remote Sensing*  
932 *Symposium (IGARSS), 2014 IEEE International*, pages 1253–1256.
- 933 Torabzadeh, H., Morsdorf, F., and Schaepman, M. E. (2014b). Fusion of imaging spectroscopy and airborne  
934 laser scanning data for characterization of forest ecosystems – a review. *ISPRS Journal of Photogram-*  
935 *metry and Remote Sensing*, 97(Supplement C):25 – 35.
- 936 Treuhaft, R. N., Asner, G. P., Law, B. E., and Van Tuyl, S. (2002). Forest leaf area density profiles from  
937 the quantitative fusion of radar and hyperspectral data. *Journal of Geophysical Research: Atmospheres*,  
938 107(D21):ACL 7–1–ACL 7–13. 4568.
- 939 Tyler, A. N., Hunter, P. D., Spyrakos, E., Groom, S., Constantinescu, A. M., and Kitchen, J. (2016). De-  
940 velopments in earth observation for the assessment and monitoring of inland, transitional, coastal and  
941 shelf-sea waters. *Science of The Total Environment*, 572(Supplement C):1307 – 1321.
- 942 Ungar, S. G., Pearlman, J. S., Mendenhall, J. A., and Reuter, D. (2003). Overview of the Earth Observing  
943 One (EO-1) mission. *IEEE Transactions on Geoscience and Remote Sensing*, 41:1149–1159.
- 944 Ustin, S. L., Roberts, D. A., Gamon, J. A., Asner, G. P., and Green, R. O. (2004). Using imaging spec-  
945 troscopy to study ecosystem processes and properties. *BioScience*, 54(6):523–534.
- 946 van der Meer, F. D., van der Werff, H. M., van Ruitenbeek, F. J., Hecker, C. A., Bakker, W. H., Noomen,  
947 M. F., van der Meijde, M., Carranza, E. J. M., de Smeth, J. B., and Woldai, T. (2012). Multi- and  
948 hyperspectral geologic remote sensing: A review. *International Journal of Applied Earth Observation*

- 949 *and Geoinformation*, 14(1):112 – 128.
- 950 Veraverbeke, S., Hook, S., and Harris, S. (2012). Synergy of vswir (0.4–2.5  $\mu\text{m}$ ) and mtir (3.5–12.5  $\mu\text{m}$ )  
951 data for post-fire assessments. *Remote Sensing of Environment*, 124(Supplement C):771 – 779.
- 952 Verhoef, W. (1984). Light scattering by leaf layers with application to canopy reflectance modeling: The  
953 SAIL model. *Remote sensing of environment*, 16(2):125–141.
- 954 Vermote, E. F., Tanre, D., Deuze, J.-L., Herman, M., and Morcette, J.-J. (1997). Second Simulation of the  
955 Satellite Signal in the Solar Spectrum, 6S: an overview. *IEEE transactions on geoscience and remote  
956 sensing: a publication of the IEEE Geoscience and Remote Sensing Society*, 35(3):675–686.
- 957 Wei, Q., Dobigeon, N., and Tourneret, J. Y. (2015). Bayesian fusion of multi-band images. *IEEE Journal  
958 of Selected Topics in Signal Processing*, 9(6):1117–1127.
- 959 Woodhouse, I. H., Nichol, C., Sinclair, P., Jack, J., Morsdorf, F., Malthus, T. J., and Patenaude, G. (2011).  
960 A multispectral canopy lidar demonstrator project. *IEEE Geoscience and Remote Sensing Letters*,  
961 8(5):839–843.
- 962 Xu, B. and Gong, P. (2007). Land-use/land-cover classification with multispectral and hyperspectral eo-1  
963 data. 73:955–965.
- 964 Yokoya, N., Chan, J. C.-W., and Segl, K. (2016). Potential of resolution-enhanced hyperspectral data for  
965 mineral mapping using simulated enmap and sentinel-2 images. *Remote Sensing*, 8(3).
- 966 Yokoya, N., Grohnfeldt, C., and Chanussot, J. (2017). Hyperspectral and multispectral data fusion: A  
967 comparative review of the recent literature. *IEEE Geoscience and Remote Sensing Magazine*, 5(2):29–  
968 56.
- 969 Yokoya, N., Yairi, T., and Iwasaki, A. (2012). Coupled nonnegative matrix factorization unmixing for  
970 hyperspectral and multispectral data fusion. *IEEE Transactions on Geoscience and Remote Sensing*,  
971 50(2):528–537.
- 972 Zilioli, E., Brivio, P., and Gomasca, M. (1994). A correlation between optical properties from satellite  
973 data and some indicators of eutrophication in lake garda (italy). *Science of The Total Environment*,  
974 158(Supplement C):127 – 133.
- 975 Zwally, H., Schutz, B., Abdalati, W., Abshire, J., Bentley, C., Brenner, A., Bufton, J., Dezio, J., Hancock, D.,  
976 Harding, D., Herring, T., Minster, B., Quinn, K., Palm, S., Spinhirne, J., and Thomas, R. (2002). Icesat's  
977 laser measurements of polar ice, atmosphere, ocean, and land. *Journal of Geodynamics*, 34(3):405 –  
978 445.